

Simulating Observations of Dark Matter Dominated Galaxies: Towards the Optimal Halo Profile

W.J.G. de Blok^{1,2}, Albert Bosma³, Stacy McGaugh⁴

¹ *Australia Telescope National Facility, PO Box 76, Epping NSW 1710, Australia*

² *Department of Physics and Astronomy, Cardiff University, 5 The Parade, Cardiff CF24 3YB, United Kingdom*

³ *Observatoire de Marseille, 2 Place Le Verrier, 13248 Marseille Cedex 4, France*

⁴ *Department of Astronomy, University of Maryland, College Park, MD 20742-2421, USA*

2 December 2024

ABSTRACT

Low Surface Brightness (LSB) galaxies are dominated by dark matter, and their rotation curves thus reflect their dark matter distribution. Recent high-resolution rotation curves suggest that their dark matter mass-density distributions are dominated by a constant-density core. This seems inconsistent with the predictions of Cold Dark Matter (CDM) models which produce halos with compact density cusps and steep mass-density profiles. However, the observationally determined mass profiles may be affected by non-circular motions, asymmetries and offsets between optical and dynamical centres, all of which tend to lower the observed slopes. Here we determine the impact of each of these effects on a variety of halo models, and compare the results with observed mass-density profiles. Our simulations suggest that no single systematic effect can reconcile the data with the cuspy CDM halos. The data are best described by a model with a soft core with an inner power-law mass-density slope $\alpha = -0.2 \pm 0.2$. However, no single universal halo profile provides a completely adequate description of the data.

Key words: galaxies: kinematics and dynamics — galaxies: fundamental parameters — dark matter

1 INTRODUCTION

Low Surface Brightness (LSB) galaxies are dominated by dark matter. Their stellar populations are dynamically unimportant and the rotation curves are thus direct tracers of their dark matter distributions (de Blok & McGaugh 1997). This is important, as in brighter galaxies it is difficult to disentangle the dynamical contributions of the dark and visible matter, and unambiguously determine the distribution of the dark matter. LSB galaxies give us a unique opportunity to compare observations with cosmological dark matter simulations.

These numerical models, based on the Cold Dark Matter (CDM) paradigm, make very specific predictions about the distribution of dark matter in galaxies (Dubinski & Carlberg 1991). In CDM halos the mass density distribution in the inner parts is characterized by a steep density “cusp”, usually described by a power-law $\rho(r) \sim r^\alpha$ with slopes varying from $\alpha = -1$ (Navarro, Frenk & White 1996, 1997) to $\alpha = -1.5$ (e.g. Moore et al. 1998, 1999; Bullock et al. 2001). This cusp manifests itself in a steeply rising rotation curve with a specific shape. Observations of dwarf and LSB galaxies (Moore 1994; McGaugh, Rubin & de Blok 2001; de Blok, McGaugh & Rubin 2001; Blais-Ouellette et al. 2001; de Blok

& Bosma 2002; Marchesini et al. 2002) show that real rotation curves rise less steeply than predicted, and do not have the required CDM shape. Similar conclusions have been reached by Salucci (2001) and Salucci & Borriello (2001) for high surface brightness disk galaxies. At small radii, the empirically determined mass distribution can be well described by a central kpc-sized constant-density core (i.e. $\alpha \sim 0$ in the inner parts) (de Blok et al. 2001; de Blok & Bosma 2002 [hereafter dBMBR and dBB02 respectively]).

dBMBR and dBB02 base their conclusions on observations of rotation curves of over 60 LSB galaxies. They determine the mass density profiles that give rise to the observed rotation curves and fit the inner parts with a single power-law. The resulting distribution of inner mass-density slopes shows a strong peak at $\alpha = -0.2 \pm 0.2$ (see Fig. 2 in dBMBR), but with a large spread, varying from steep and cuspy $\alpha = -2$ profiles to flat and even moderately positive slopes. This was interpreted as a result of resolution effects: dBMBR find that the best resolved curves show the flattest profiles (see Fig. 3 in dBMBR and Fig. 14 in dBB02), contrary to what is expected for CDM. At lower resolutions the CDM and the ISO models both predict the same slopes, leading to an ambiguity as to which model fits lower resolution data best (van den Bosch & Swaters 2001).

arXiv:astro-ph/0212102v1 4 Dec 2002

However, resolution is not the only effect that can influence the measured slopes. Other effects, which dBMBR and dBB02 did not thoroughly investigate, include non-circular motions, offsets between dynamical and optical centres, lopsidedness, asymmetries, and slit-width. These effects all have the potential to decrease the measured inner mass-density slopes. It is thus important to investigate if the observed shallow slopes truly reflect the underlying mass distribution, or whether they are determined by systematic effects. For example, small offsets between the dynamical centre and the optical centre are sometimes observed in late-type barred galaxies (Pisano, Wilcots & Elmegreen 1998; de Vaucouleurs & Freeman 1972). If this were a systematic property of all LSB or dwarf galaxies then observations aligned on the optical centre would not necessarily probe the dynamical centre. Even if the galaxy in question had a steep CDM density cusp at the dynamical centre, the derived slope would be shallower, giving the impression of a core-dominated halo. Hence these systematic effects should be understood, in order to judge whether LSB galaxies have cuspy or core-dominated halos. Furthermore, once the impact (if any) of these systematic effects is understood, one could hope to determine how much they contribute to the scatter in the observed slopes, and whether the range in observed slopes can be attributed to “cosmic scatter” or whether a single halo profile for all galaxies suffices.

In this paper we investigate the importance of these systematic effects by deriving a large ensemble of rotation curves of both cuspy CDM and core-dominated (simulated) halos, using observed curves as a constraint. We apply the relevant systematic effects to these simulated curves, and then determine the inner mass-density slopes. Our main conclusion is that none of the systematic effects investigated can convincingly wipe out the signature of a CDM halo. In other words, if LSB galaxies had CDM halos, they would be unambiguously detectable, even in the presence of systematic effects. The most likely interpretation is that the observed core-dominated mass-distribution reflects the true dark matter distribution in LSB galaxies.

The organization of this paper is as follows. Section 2 discusses some aspects of the observational comparison sample. Section 3 describes the simulations. Section 4 contains the results of simulations that include various systematic effects. In Sect. 5 we describe some tests performed with real data, while in Sect. 6 we attempt to use the simulations to improve on the halo model used. In Sect. 7 we present our conclusions.

2 DATA

The model rotation curves we derive will be compared with the results presented in dBMBR and dBB02. The focus will be on the histograms of the inner slope α (dBMBR, their Fig. 2) and the diagrams of inner slope α versus resolution r_{in} of the rotation curve (dBMBR, their Fig. 3 and dBB02, their Fig. 14). These diagrams are based on power-law fits to the inner parts of the mass-density profiles derived from the ~ 60 high-resolution rotation curves from McGaugh, Rubin & de Blok (2001), de Blok, McGaugh & Rubin (2001) and dBB02. These rotation curves are measured from long-slit H α spectra, mostly sampling the kinematics in the inner

parts, in many cases combined with lower-resolution H I rotation curves sampling the outer parts (de Blok, McGaugh & van der Hulst 1996).

2.1 Defining a restricted sample

These data span a large range in resolution, inclination, and general quality of the rotation curves. It is therefore worth asking whether the data themselves may in any way be biased by systematic effects. For example, if all the core-like profiles found turned out to have been derived from low-resolution, low-quality rotation curves, one would have valid reasons to question the usefulness of those data and conclusions based on them.

McGaugh, Barker & de Blok (2003) present such an analysis where they analyse only those rotation curves that resemble NFW CDM rotation curves best, and conclude that there is no systematic difference in the distributions of c for their restricted and total samples.

Here we make a similar comparison, but concentrate on the properties relevant for our comparison with simulations, namely distributions of c and the inner slope α . Starting with the complete sample from dBMBR and dBB02 (see Fig. 1), we apply the following cuts: firstly, we remove all galaxies with inclinations $i < 30^\circ$ and $i > 85^\circ$. This leaves 44 galaxies. The resulting distribution is insensitive to the choices for the upper and lower inclination limit: we have tried cuts with lower limits of 25° and 40° , and upper limits of 75° and 80° , and find almost identical distributions. Secondly, we remove all galaxies with low-quality rotation curves, i.e. with a small number of independent data points, with large error-bars, and large asymmetries. Galaxies where the minimum-disk assumption is clearly not valid were removed as well (e.g. UGC 6614). The resulting sample contains 39 galaxies. Finally, as the difference between cusp and core is most clearly visible in the innermost part of the galaxies, we demand that the inner part is resolved: we retain only those galaxies that have at least 2 independent data points in the inner 1 kpc. This leaves us with a final sample of 19 galaxies, listed in Table 1 and shown in Fig. 1.

A comparison of the different stages of pruning shows no systematic differences between the distributions of the initial full sample and final restricted sample. If anything, the peak of the distribution of inner slopes α has shifted towards a more positive value. The tail towards negative slopes has disappeared. The peak in the c -distribution still occurs near $c \sim 6$, and the peak at $c \sim 0$ is still present in the final sample.

2.2 Comparison with literature

Recently, Swaters et al. 2002 [hereafter SMBB] have made a similar analysis of a sample of 15 dwarf and LSB galaxies. They reach the conclusion that the inner mass density slopes in their sample cover the full range $-1 \lesssim \alpha \lesssim 0$, but claim that though their data prefer a shallow $\alpha \sim 0$ slope, they cannot rule out steep $\alpha = -1$ slopes for their sample. The analysis presented in the previous section and in dBMBR suggests that a large fraction of the steep slopes one finds are actually due to insufficient resolution. It would thus be interesting to see if these effects are also present

in the SMBB data. We subjected their data to the same quality criteria that we used for ours. In practice this meant that 5 galaxies with less than 2 independent points in the inner kpc were rejected (F563-V2, F568-1, F568-3, F568-V1, F574-1), as well as one galaxy (U5721) where the minimum disk assumption is invalid. A high-resolution optical velocity field of U5721 (Garrido et al. 2002) clearly shows the presence of a kinematical minor axis not perpendicular to the major axis. This is a classical indication of an oval distortion (Bosma 1978). For this galaxy, there are images in the HST archive that show the presence of a weak bar (see also dBB02, their Sec. 9.2.2., noting that U5721 is also known as N3274).

We are thus left with 9 well-resolved rotation curves. Our restricted sample has three galaxies in common with this restricted SMBB sample. We find that for two of these galaxies the measured slopes are consistent at better than 1σ (UGC 731 and UGC 4325). For one galaxy (UGC 11557) the slopes differ significantly: SMBB find $\alpha = -0.84 \pm 0.27$, while dBBMR find $\alpha = -0.08 \pm 0.23$. An inspection of the density profiles in Fig. 1 of dBBMR and Fig. 5 in SMBB shows that this difference in slope is entirely due to a different choice of break radius, where SMBB have chosen a larger radius than dBBMR, resulting in a much steeper slope. Choosing a smaller break radius will give a value entirely consistent with that in dBBMR. An inspection of the break radii of the 8 other high-resolution SMBB profiles shows that UGC 11557 is the only case where we would claim that the choice in break radius is ambiguous. We have overplotted the distribution of slopes of the restricted SMBB sample in Fig. 1. The number of galaxies is small, so it is difficult to say anything about the intrinsic distribution of slopes, but it is clear that the SMBB sample is entirely consistent with our larger restricted sample (and even more so when the ambiguous slope for UGC 11577 is removed).

Contrary to the conclusions reached by SMBB we do not find that edge-on or barred galaxies skew the distribution of slopes. A comparison between our full and restricted samples shows the inclusion or omission of edge-on galaxies does not shift the average value of the slope significantly from $\alpha \sim -0.2$. We also note that edge-on late-type galaxies are expected to be transparent (Bosma et al. 1992; Matthews & Wood 2001); furthermore the $H\alpha$ spectra from which the rotation curves are derived do not show the broad velocity wings expected when projection effects play a large role.

Conclusions regarding the importance of bars are more ambiguous as these depend on what one defines as a bar. Certainly none of the galaxies investigated here contain the dominant straight bars found in earlier-type galaxies. Here we are mostly dealing with Magellanic-type oval components, and it is obviously a matter of judgement to decide whether one deals with an intrinsically oval component, or a projected more circular one.

SMBB list which of the galaxies in their sample they consider barred. In order to make a consistent barred/non-barred division of the galaxies in our restricted sample, we use their results to gauge and calibrate our classification. That any such classification remains uncertain is illustrated by the fact that none of the galaxies in the SMBB sample are classified in NED as unambiguously barred (Hubble type SB), *except* UGC 2259 [Hubble type SB(s)dm]. SMBB classify this galaxy as *unbarred*, even though the bar with

perpendicular spiral arms is easily visible on the Digital Sky Survey image. The inner mass-density slope found for this galaxy is steep at $\alpha = -0.86 \pm 0.18$. As bars are disk dynamical features (e.g., Athanassoula 2002), they imply a significant disk mass. Such heavy disks more than compensate for any underestimate of the slope which might be caused by the noncircular motions they induce. The minimum disk assumption fails, and with it the steep halo slopes inferred in this extreme limit.

Despite this UGC 2259 discrepancy, we have used the SMBB results to gauge which of the galaxies in our restricted sample should be classified as barred. We list our classification in Table 1; we find 13 non-barred galaxies, 5 barred galaxies and 1 ambiguous case.

The galaxies in our restricted sample have been selected not to suffer from inclination effects or projection effects. The majority of them is unbarred, and it is not obvious at all that the presence of a bar influences any of the results. This comparison of restricted samples shows that once a proper pruning is made to only include minimum-disk, well-resolved galaxies, most of the differences are merely a matter of semantics. The observed *shallow* inner mass-density slopes of LSB and dwarf galaxies do therefore reflect the intrinsic properties of their potentials.

3 MODELS

3.1 Model rotation curves

In order to model the various effects that can affect rotation curves we use the full expression for the observed line-of-sight velocity at any position in a galaxy velocity field. This is given by (see Fig. 2):

$$V(x, y) = V_0 + V_C(R) \sin i \cos \theta + V_{\text{exp}}(R) \sin i \sin \theta \quad (1)$$

where $V(x, y)$ is the observed velocity at position (x, y) , where we define the dynamical centre of the galaxy to be at $(0, 0)$; V_0 is the systemic velocity, which is not relevant in this analysis and which will be ignored; $V_C(R)$ is the actual rotation curve velocity at radius R , where R is measured in the plane of the galaxy. $V_{\text{exp}}(R)$ is an expansion velocity describing non-circular motions (which can be used to describe e.g. streaming motions). Position (x, y) is measured in the plane of the sky. We additionally define the radius r as the projection of R on the plane of the sky. As usual, i is the inclination. Following Begeman (1987) we define a coordinate system with the $+X$ direction towards decreasing right ascension, the $+Y$ direction towards the north, and the dynamical centre as origin. Position angles in the plane of the sky are measured from N towards E. The major axis of the galaxy has sky position angle ϕ . Position (x, y) then has position angle θ with respect to the major axis as measured in the plane of the galaxy given by:

$$\begin{aligned} \cos \theta &= \frac{-x \sin \phi + y \cos \phi}{R} \\ \sin \theta &= \frac{-x \cos \phi - y \sin \phi}{R \cos i}. \end{aligned} \quad (2)$$

We now introduce the angle ϕ' which is the sky position angle of position (x, y) . We can express x and y as

$$x = -r \cos\left(\frac{\pi}{2} - \phi'\right) = -r \sin \phi'$$

$$y = r \sin\left(\frac{\pi}{2} - \phi'\right) = r \cos \phi'. \quad (3)$$

Combining this with Eqs. (2) gives

$$\begin{aligned} \cos \theta &= \frac{r}{R} (\sin \phi' \sin \phi + \cos \phi' \cos \phi) \\ \sin \theta &= \frac{r}{R \cos i} (\sin \phi' \cos \phi - \cos \phi' \sin \phi). \end{aligned} \quad (4)$$

Without loss of generalisation, we can make the simplifying assumption that the major axis coincides with the X -axis, so that $\phi = \pi/2$, as sketched in Fig. 2. Equation (4) then reduces to $\cos \theta = (r/R) \sin \phi'$ and $\sin \theta = -(r/(R \cos i)) \sin \phi'$.

We are now in a position to derive the line-of-sight velocity at any position (x, y) , given any rotation curve V_C and non-circular motion component V_{exp} . For example, Fig. 2 shows a slit positioned parallel to the major axis, but offset by an amount y . Assuming that $V_{\text{exp}} = 0$ everywhere, the observed line-of-sight velocities along the slit are derived by varying x at a constant y , for a given input $V_C(R)$ and known i . The radii $R = \sqrt{x^2 + (y/\cos i)^2}$ and $r = \sqrt{x^2 + y^2}$ can be calculated, as can the position angle $\phi' = \arctan(y/x)$, so that θ can be derived. This then trivially gives the line-of-sight velocities. One last step we need to take, in order to “simulate” our ignorance regarding the systematic effects in this particular example, is to associate the positions along the slit x (rather than the radii r) with the derived line-of-sight velocities, because, as with real data, these curves will be analysed under the assumption that no systematic effects are present. Other situations, including non-circular motions, can be modeled in a similar way, as shown below.

3.2 Halo models

For $V_C(R)$ we will initially investigate two halo models, apply identical systematic effects to both, and determine the resulting rotation curves and mass-density profiles. The first model is the so-called NFW halo, favoured by the CDM simulations, but seemingly not by the observations. The other model is the pseudo-isothermal halo, preferred by observations, but without any basis in cosmology. The properties of these models are summarised below.

3.2.1 NFW halos

The internal structure of DM halos formed in a CDM universe was investigated in detail by Navarro, Frenk & White (1996, 1997). They found that the halos modeled in their N-body simulations could be well described by

$$\rho(R) = \frac{\rho_i}{(R/R_s)(1 + R/R_s)^2} \quad (5)$$

where R_s is the characteristic radius of the halo and ρ_i is related to the density of the universe at the time of collapse. The density and radius are strongly correlated with the mass of the halo. At small radii the density diverges as r^{-1} . This mass distribution gives rise to a halo rotation curve

$$V_C(R) = V_{200} \left[\frac{\ln(1 + cx) - cx/(1 + cx)}{x[\ln(1 + c) - c/(1 + c)]} \right]^{1/2}, \quad (6)$$

where $x = R/R_{200}$. The radius R_{200} is the radius where the density contrast exceeds 200, roughly the virial radius

(Navarro, Frenk & White 1996). The characteristic velocity V_{200} of the halo is defined in the same way as R_{200} . The curve is characterised by two parameters: a concentration c and a velocity V_{200} . These are not independent, but related through the assumed cosmology. For a standard Λ CDM this relation can be well described as

$$\log c = 1.191 - 0.064 \log V_{200} - 0.032 \log^2 V_{200} \quad (7)$$

(cf. Navarro, Frenk & White 1997). This relationship has an associated scatter, but estimates in the literature differ. Here we adopt a conservative logarithmic scatter of $\sigma(\log c) = 0.18$ (Bullock et al. 2001). Note that in a more recent paper Wechsler et al. (2002) advocate a scatter of $\sigma(\log c) = 0.14$. As the precise value of the scatter is not critical for our results, we use the larger value in order to give the maximum amount of leeway to the CDM models. See de Blok, McGaugh & Rubin (2001) for more details.

Recent N-body simulations have found even steeper inner mass-density slopes of $\alpha = -1.5$ (Moore et al. 1998). We will not consider these steeper slopes here; the NFW model can be regarded as a limiting case. If the data do not admit $\alpha = -1$ slopes, they certainly will not allow $\alpha = -1.5$ values.

In Fig. 3 we show the inner part of the velocity field of a massless disk in a NFW halo with $c = 8.6$ (i.e. approximately the typical value predicted by Λ CDM, see McGaugh, Barker & de Blok 2003) and $V_{200} = 100 \text{ km s}^{-1}$. The iso-velocity contours show a characteristic “pinch” in the very inner parts, which is a signature of the NFW profile.

3.2.2 ISO halos

The spherical pseudo-isothermal (ISO) halo differs from the NFW halo in that it has a central region with a constant density. Its density profile is

$$\rho(R) = \frac{\rho_0}{1 + (R/R_C)^2}, \quad (8)$$

where ρ_0 is the central density of the halo, and R_C the core radius of the halo. The corresponding rotation curve is given by

$$V_C(R) = \sqrt{4\pi G \rho_0 R_C^2 [1 - (R_C/R) \arctan(R/R_C)]}. \quad (9)$$

The ISO halo is characterised by any 2 out of 3 parameters: an asymptotic velocity V_∞ , a core radius R_C and a central density ρ_0 . These parameters are related through

$$V_\infty = \sqrt{4\pi G \rho_0 R_C^2}. \quad (10)$$

Fig. 3 shows the inner part of a velocity field of a massless disk embedded in an ISO halo with $V_\infty = 100 \text{ km s}^{-1}$ and $R_C = 1 \text{ kpc}$. The iso-velocity contours are much rounder, and do not show the “pinch” of the NFW velocity field.

3.3 Simulations

In order to be able to directly compare the simulations with the data it is important that the simulated halos are “realistic”, in the sense that the range of halo parameters for the NFW model needs to be similar to that found in the simulations (which are constructed to resemble the real Universe),

whereas the ISO halo parameters need to resemble those determined from observations. We therefore use the following boundary conditions in the models.

(i) *halo parameters.* For the NFW halos we take a random value for V_{200} between between 20 and 490 km s^{-1} , and compute the corresponding c -value using Eq. 7, modified by a random scatter as described above. To simulate ISO halos we choose a random value for V_∞ between 30 and 300 km s^{-1} , roughly corresponding to the observed range in galaxy maximum rotation velocities. For ρ_0 we choose a random value from the uniform range $\log(\rho_0/[M_\odot \text{pc}^{-3}]) = -1.7 \pm 0.4$ (Firmani et al. 2000). The core radius R_C is then determined using Eq. 10.

(ii) *inclination.* A random axis-ratio is chosen in the range from 0.17 to 0.76, corresponding to inclinations between 40° and 80° . The inclination has no direct effect on the slopes, but serves as a scale factor in the error-bars determined below, and hence the uncertainty in the slopes.

(iii) *physical resolution.* For each simulated galaxy the resolution in kpc at which it will be “observed” is determined as follows. Figure 4 shows the logarithmic distribution of observed resolutions (radii r_{in} of the innermost points of the rotation curves) from dBMBR and dBB02. This distribution is well approximated by a Gaussian with an average $\mu(\log r_{\text{in}}) = -0.45$ and a dispersion $\sigma(\log r_{\text{in}}) = 0.41$. The 2σ spread in resolution thus varies from 0.05 kpc to 2.3 kpc, reflecting both the spread in distance as well as the mix of optical and H I curves used. Though the precise parameters of this distribution are not critical, choosing a resolution distribution that is approximately equal to the empirical one means we can make a direct comparison between the simulations and observations.

(iv) *error-bars.* To simulate the uncertainties in the data, we de-correct the rotation curve for inclination and add error-bars. Figure 5 shows the distribution of the observational uncertainties in the dBB02 data, not corrected for inclination. The best-fitting Gaussian has an average $\mu(\log \Delta V) = 0.629$ and a dispersion $\sigma(\log \Delta V) = 0.437$. As in dBB02 and de Blok, McGaugh & Rubin (2001) we impose a minimum error of 4 km s^{-1} on the data. We draw error-bars from this distribution and assign them to the data points in the simulated rotation curve. The curve is then corrected back for inclination, thus enlarging the error-bars and uncertainty accordingly. As the intensity of the H α line is generally inversely correlated with the magnitude of the error-bar, this procedure assumes a random distribution of H α intensities. This is likely to be simplistic, but any improvement involves assuming a specific H α intensity distribution, meaning the models would lose some of their generality.

(v) *slit width.* Equation 1 gives the line-of-sight velocities along an infinitely thin slit. In reality, the observations have used a finite slit with a width of $\sim 1''$. We therefore integrate Eq. 1 over a width of $1''$ and determine the average value of $V(x, y)$ at each position along the thick slit.

(vi) *mass density profiles.* The mass density profiles are determined exactly as described in dBMBR, with one difference: dBMBR choose a “break radius” to determine the inner slope. Here we determine the slope by performing a weighted fit to the innermost 3 points. The uncertainty in the slope is determined in the same manner as in dBMBR. We have tested fitting to the innermost 2, 4 or 5 points but

this did not change any of the conclusions appreciably. We assume a spherical halo and minimum disk, i.e. the dynamical significance of the stellar disk is assumed to be negligible and the stellar mass-to-light is set to zero. For LSB galaxies minimum disk is in general a good assumption (e.g. de Blok & McGaugh 1997). It is difficult to estimate what effect the stellar disk has on the halo, but most likely the halo becomes more concentrated under the influence of the disk. In the absence of applicable models we will not explicitly simulate this, except to note that because of the dynamical insignificance of the disk the effect is likely to be small. The minimum disk assumption also gives a hard upper limit on the value of the slope, as taking into account any contribution by the stars to the mass-density slope reduces the implied dark matter slope, independent of whether any contraction has taken place or not.

(vii) *small-scale deviations.* The model rotation curves can by necessity be nothing more than pale imitations of those of real galaxies. One of the features of real rotation curves are the “bumps and wiggles”, caused by, among others, streaming motions along spiral arms, random motions of H II regions, and gas motions due to the effects of star formation. The magnitude and importance of these effects are of course different for different galaxies. They do undoubtedly play a role in the observed LSB galaxies rotation curves, but without modeling individual galaxies in detail it is impossible to determine and apply these effects to the models in an unbiased and general manner. We will return to this matter in Sect. 4.2. It should be noted though that the many ways in which rotation curves can be derived are all designed to remove the effects of these small-scale deviations: for example, the tilted ring procedure averages velocities over rings at a certain radius, whereas long-slit rotation curves use the independent information from radii at the approaching and receding sides of the galaxy to derive the underlying global rotation velocities. Our omission of these deviations means that the uncertainties we derive in our simulations will be smaller than found in the data, but this is a small price to pay not having to introduce ill-constrained random motions that may bear no resemblance with reality. A specific example will be discussed in Sect. 4.2.

4 RESULTS

4.1 Comparison with models

For each set of input parameters described below we compute 600 rotation curves per halo model. This is significantly more than the 61 observational data-points available, but avoids small number statistics affecting the simulated histogram. To compare the data and the simulations we scale the maximum of the data histogram to that of the simulation histogram. To indicate the uncertainties in the data histogram we over-plot an error-bar on each observed histogram bin which reflects the uncertainty due to counting statistics in the observational sample (these error-bars are also scaled) (see Fig. 6 for examples). In the diagram of inner slope α versus resolution r_{in} we show observational data points in the background, with the simulation results over-plotted. To avoid cluttering the plot we do not always show all 600 galaxies, but select 61 galaxies (i.e. equal to the

number of observed data points) at random (see Fig. 6 for examples).

In order to isolate the investigated systematic effects from resolution effects, we distinguish in the histograms between well-resolved galaxies (2 or more independent points per kpc; cross-hatched histogram) and less well-resolved galaxies (less than 2 independent points per kpc; single-hatched histograms). The cross-hatched histograms can be directly compared with the well-resolved sample in Fig. 1.

4.2 The Null-case

We first investigate the case of observations without any systematic effects. That is, we determine the major-axis curves defined by Eq. 1 and the ISO and NFW halo models, and follow the procedure described in Sect. 3.3. We assume there are no non-circular motions and no mismatches of any kind. The results are shown in Fig. 6. As expected, the derived slopes are close to the theoretical values. The NFW model shows a pronounced peak at $\alpha = -1$. The finite width of the slit hardly affects the measured slopes. Similar conclusions apply to the ISO model. The high-resolution ISO models show a clear $\alpha = 0$ slope, while the least-resolved models show steeper slopes, comparable to those found in the NFW model at similar resolutions.

The histograms show only partial agreement with the data. The peak occurs at the wrong value for the NFW model, and the histogram has the wrong shape. For the ISO model the peak occurs at roughly the correct value, but the shape of the histogram differs significantly from the data. Clearly some sort of effect, whether cosmic or systematic, is needed to make the simulations more consistent with the data. It is clear though that this effect needs to be more pronounced for NFW than for ISO.

4.2.1 Small-scale deviations

The simulated error-bars in Fig. 6 are smaller than those of the data. As discussed in item (vii) in Sect. 3.3, this is most likely due to the fact that we do not simulate small-scale features in the rotation curves. This does however not affect the conclusions we can draw from the simulations. After all, when averaged over ~ 60 rotation curves, we can regard the “bumps and wiggles” as essentially random: they introduce scatter but are expected to average out and will not affect the shape in a systematic way. Another reason not to include the small-scale deviations is that every galaxy is unique and has features in the rotation curve that depend on the positions of the H II regions, spiral arms, star formation etc. Given the low star formation rates, small number of H II regions, and lack of pronounced spiral arms, it is unclear how important any of these effects are in LSB galaxies compared to “normal” galaxies. It is therefore difficult to derive a universally applicable description short of modeling each galaxy individually, which is clearly unfeasible.

We illustrate the fact that small scale deviations most likely do not affect the conclusions, but merely introduce more scatter, by investigating a naive (and probably too simplistic) description for the deviations which we then apply to the simulations presented above. Fig. 7 shows a histogram of the deviations of the raw observed rotation curves

with respect to the smooth rotation curves as presented in Fig. 7 of dBB02 and Fig. 1 of de Blok, McGaugh & Rubin (2001). The deviation histogram is well described by a function of the form $\exp -|\Delta V|$. If the deviations in the rotation curves were radially uncorrelated we could add deviations derived from this distribution to our model curves, use this modified model curve to determine the underlying smooth rotation curve and subsequently measure the mass profile.

However, in real galaxies the small-scale deviations are correlated: if e.g. streaming motions along a (resolved) spiral arm cause a data point to lie above the average curve, then the data point next to it is more likely to lie above it as well. Furthermore, the deviations are defined with respect to the underlying curve, in that the latter is derived by minimising the former. Ideally, we would have to introduce an extra step in the simulations to adjust the model rotation curves to the effect of the deviations. On the other hand, as we would afterwards be fitting to the underlying curve as defined by a minimisation of deviations, and *not* to the raw deviations, their impact on the results would have to be significantly less than suggested by Fig. 7. It is thus not clear whether taking small-scale deviations into account would have a significant effect.

As a crude attempt to show these effects, we have applied to the two simulations described above, small-scale deviations drawn from the distribution shown in Fig. 7. In order to introduce a degree of correlation between the deviations, we boxcar-smooth over four data points. With real data the next step would have been to fit an underlying smooth curve by minimizing the residuals, followed by the derivation of the mass profile from the smooth curve. To determine the mass profiles we thus prefer not to use the raw data, since the mass profile derivation uses the gradient of the rotation curve. Instead we introduce a bit of binning and smoothing to determine the underlying gradient. In practice, we thus have to soften the impact of the derived (unbinned) deviations on the simulated curves. Here we (arbitrarily) divide them by a factor of four before adding. The number of data points to smooth over as well as this softening factor were found empirically by demanding that the error bars in the simulated slopes match those of the data. Fig. 8 shows the results. The method has introduced scatter, but not changed the conclusions that were derived from the simulations presented in Fig. 6.

It is clear that the method described above is unsatisfactory. The smoothing and softening factors are arbitrary and ill-constrained and the amount of scatter introduced depends strongly on the values one assumes for them. Again, the lack of a universally applicable description of what are essentially stochastic and random processes makes this an unfeasible exercise. Furthermore, as the derivation of rotation curves uses extra information such as continuity and symmetry between approaching and receding sides it is not clear whether the net impact would be significant. Therefore, rather than trying to fine-tune a clearly unsatisfactory description we prefer to proceed without it, keeping in mind that there is this missing ingredient, but that it is not likely to affect the conclusions in a significant way.

4.3 Lopsidedness and asymmetries

One of the assumptions made in rotation curve analysis is that the velocity field is symmetrical around the dynamical centre. This is not necessarily the case for all galaxies; some seem to have a “kinematical lopsidedness” (see e.g. Swaters et al. 1999 for an extensive description), where the rotation curves of the approaching and receding sides each have different slopes and amplitudes (cf. Fig. 2 in Swaters et al. 1999). The amplitudes of the curves can differ by up to 20 per cent. Interestingly, kinematical lopsidedness does not seem to automatically imply a spatial offset between optical and dynamical centres. Kinematical lopsidedness can thus affect the interpretation of mass-density slopes.

Here we investigate the effect of kinematical lopsidedness on the rotation curves of NFW and ISO halos. We model the lopsidedness by computing a rotation curve, but choose an incorrect point of symmetry (or incorrect systemic velocity). After flipping the rotation curve around this incorrect point of “symmetry” we thus end up with approaching and receding side curves that have different amplitudes and shapes, and therefore different inner slopes. We then proceed to take the average of the inner curves, and determine the mass-density profile.

As the derived slopes are steepest when the point of symmetry is chosen correctly, this procedure will flatten the measured slopes. Figure 9 shows an example of a “kinematically lopsided” NFW curve. This procedure does not take into account the observed behaviour of the curves at large radii (see e.g. N4395 in Swaters et al. 1999; here one side of the galaxy exhibits a rising rotation curve, while at identical radii on the other side it has already flattened), but as our interest is in the inner slope, this will not affect any of the conclusions.

We assume offsets of 0.1, 0.5 and 1 kpc. Note that though the magnitude of the effect is expressed in kpc, we do not imply that this involves a shift in dynamical centre. Our notation is merely a convenient way to express the incorrect choice of systemic velocity that we use to create the kinematical lopsidedness. The offsets used here result in average in velocity offsets of ~ 15 , ~ 30 and $\sim 50 \text{ km s}^{-1}$ respectively (see bottom row in Fig. 10). We also assume that there are no additional offsets between optical and dynamical centres.

Figure 10 shows the results for the NFW halos. We see that lopsidedness is not important as long as the effect occurs on scales smaller than the resolution. A lopsidedness of between ~ 0.5 and ~ 1 kpc (which translates into an average velocity shift of $\sim 40 \text{ km s}^{-1}$) is needed in order to bring most of the NFW points into the $\alpha = 0$ part of the diagram. The peak at $\alpha = -1$ in the 0.1 kpc case is caused mainly by well-resolved galaxies. Small offsets are thus inconsistent with NFW models. This peak is still present in the 0.5 kpc case, but is now mainly caused by lower resolution galaxies. The well-resolved galaxies are distributed more like the observed histogram, but with an excess of galaxies with positive slopes. The spread in slopes at these higher resolutions is much larger than observed. Large offsets of ~ 1 kpc are inconsistent with the observed distribution as nearly all well-resolved galaxies exhibit too positive slopes.

The bottom-row in Fig. 10 show the distribution of the velocity differences between approaching and receding side (not corrected for inclination) for the various offsets. Also

shown is the distribution of the same differences but as a fraction of the halo velocity V_{200} .

In order to explain the data with NFW models, one thus needs to assume a net lopsidedness for *all* galaxies of ~ 30 to $\sim 60 \text{ km s}^{-1}$. Estimates of the fraction of galaxies that are kinematically lopsided reach up to 30 to 50 per cent (Swaters et al. 1999), but with much smaller velocity differences. It is thus not possible to explain the data with CDM models in combination with lopsidedness alone. We do not show the ISO halo results: ISO halos already show a slope that is slightly more positive than the data (Fig. 6), adding in extra flattening due to lopsidedness results in even more positive slopes. ISO halos are thus not consistent with a large (i.e. shift in symmetry point $\gtrsim 1$ kpc) kinematical lopsidedness.

4.4 Non-circular motions

A frequently made assumption is that the visible matter in a galaxy is on circular orbits, and therefore that the measured line-of-sight velocities represent the true rotation velocity. If, however, part of the measured velocity is due to non-circular motions, it is no longer representative indicator of the mass content of a galaxy. Systematic non-circular motions are most commonly observed as streaming motions along bars or spiral arms (we do not consider local non-circular motions due to e.g. star formation or supernovae, as explained in Sect. 3.3 and 4.2). Bright galaxies can show large streaming motions: e.g. $\sim 30 \text{ km s}^{-1}$ in M81 (Adler & Westpfahl 1996) or $\sim 20 \text{ km s}^{-1}$ in NGC 1365 (Jörsäter & van Moorsel 1995). These galaxies are however mostly grand-design spirals with pronounced spiral structures. Streaming motions in late-type spirals such as M33, NGC 300, NGC 925 or NGC 1744 are found to be much smaller, and barely distinguishable from random motions in the disk (i.e. $\lesssim 10 \text{ km s}^{-1}$) (Deul & van der Hulst 1987; Puche, Carignan & Bosma 1990; Pisano, Wilcots & Elmegreen 1998). LSB galaxies are similar to these late-type galaxies and would not be expected to have large circular motions. H I velocity fields also show no evidence for large systematic non-circular motions $\gtrsim 10 \text{ km s}^{-1}$ (de Blok, McGaugh & van der Hulst 1996; Weldrake, de Blok, Walter 2002).

We model non-circular streaming motions by introducing a radial velocity component (see Eq. 1). The effects of streaming motions on a rotation curve are strongest when they are oriented parallel to the minor axis. We approximate this by adding a constant velocity component to the rotation curve over the inner one-third of its radius (the exact range is not important as we use only the inner points to determine the mass-density profile). We thus use Eq. 1 but change the phase of the radial component by $\pi/2$. Again we only show the results for the NFW halos, as the ISO halos are only consistent with no or very small non-circular motions, for the same reason as with kinematical lopsidedness: their profiles are already slightly flatter than the data, and more flattening is not needed.

We have computed models for streaming velocities of 5, 10 and 20 km s^{-1} . Figure 11 shows that systematic streaming motions of order $\sim 20 \text{ km s}^{-1}$ are needed to at least partially explain the data for the well-resolved galaxies with a NFW halo. There is however still an excess of data points

with slope $\alpha = -1$ formed of low-resolution galaxies, as well as an excess of positive slopes due to well-resolved galaxies. The bottom row in Fig. 11 shows that for a significant fraction of the galaxies a streaming motion of this magnitude amounts to ~ 20 per cent or more of the halo velocity V_{200} . In order to use streaming motions in combination with NFW halos, one thus needs to assume that *all* galaxies have systematic non-circular motions over a large part of the disk of order $\sim 20 \text{ km s}^{-1}$. This contradicts the observational data for late-type galaxies.

4.5 Mismatched position angles

A mis-match between the true position angle and the observed position angle does not lead to a change in slope for axisymmetric potentials. As can be seen from Eq. 1 it will merely introduce a scale-factor of order $(\cos\theta/\cos\theta')$ where θ and θ' are the true and mis-matched position angles respectively. In the absence of non-circular motions and in axisymmetric potentials one can even correct for a mis-matched position angle. If the mass-distribution in the central parts is not axisymmetric, then the precise value of the position angle becomes important. However, in these cases the inner parts of the galaxy are likely to be dominated by the stellar component, or the halo is very triaxial. In these cases the minimum disk and spherical halo assumptions are no longer valid. One needs to make self-consistent multi-component galaxy models, and can no longer use the simple one-component models we have been using.

4.6 Offsets between dynamical and optical centres

It is generally assumed that in a galaxy the optical centre and the dynamical centre coincide. If, however, this is not the case, then, at least for NFW halos, measuring the kinematics around the optical centre will lead to the impression that the slope of the inner mass density profile is shallow rather than steep.

It is known that in some late-type (barred) galaxies the optical centre can be located up to ~ 1.5 kpc away from the dynamical centre (Pisano, Wilcots & Elmegreen 1998; de Vaucouleurs & Freeman 1972; Weldrake, de Blok, Walter 2002). This ‘‘morphological lopsidedness’’ is different from the kinematical lopsidedness discussed before, in that as long as the stellar population is unimportant, the potential can still be dominated by the halo and be axisymmetric around the dynamical centre. It should be stressed though, that for the majority of bright galaxies where the kinematics have been investigated in detail, the optical centre and dynamical centre do coincide (cf. Begeman 1987). In these galaxies the slit would sample the true dynamical centre.

To model the effect of offsets between dynamical and (observed) optical centers, we run the simulations assuming a distribution of offsets and observe the halos with a slit offset from the dynamical center (see Fig. 2). We assume Gaussian distributions of offsets with dispersions $\sigma = (0.5, 1, 2, 3, 4, 5, 6)$ arcseconds. For each of these seven cases we run the simulations twice, once producing 600 NFW halos and once producing 600 ISO halos. As an offset between dynamical and optical center is equivalent to a slit offset, we draw a random slit offset from the relevant Gaussian offset

distribution for each halo (i.e. the first case produces 600 NFW and 600 ISO halos, each observed with offset slits, where the distribution of slit offsets was Gaussian with a dispersion $\sigma = 0.5''$, and so on for all other values of the dispersion). We have also modeled uniform distributions using widths identical to the dispersions listed above, with identical conclusions as the Gaussian distributions.

4.6.1 NFW halos

In Fig. 12 a random selection of 10 rotation curves derived assuming a Gaussian offset distribution with $\sigma = 5''$ is shown in comparison with the corresponding no-offset rotation curves. Also shown are the corresponding mass density profiles. For the average distance of the observed sample of ~ 73 Mpc, this dispersion corresponds to a physical dispersion of ~ 1.8 kpc. We use such a large offset dispersion to clearly show the differences between the curves, which would hardly be visible for smaller dispersions.

The $r_{\text{in}} - \alpha$ comparison is shown in Fig. 13. The observed and theoretical distributions are distinctly different, as also seen in the histograms in Fig. 14. The NFW models show a pronounced peak at $\alpha = -1$ not seen in the data. The high-resolution and low-resolution histograms look very similar. The only way to explain the observed distribution with NFW halos and centre offsets is to assume that for all galaxies observed the position of the dynamical centre is offset from the optical centre by $\sigma \sim 3-4''$. At higher dispersions the distributions becomes too biased towards $\alpha = 0$. We can put this in context by comparing with the average scale length of the F-LSB galaxies in de Blok, van der Hulst & Bothun (1995), which is $11.0''$. Compared to the sizes of the optical disks, the offsets needed are thus significant. For uniform offset distributions similar conclusions can be derived.

4.6.2 ISO halos

In Fig. 15 a random selection of 10 rotation curves derived assuming the ISO model and a Gaussian offset distribution with $\sigma = 2''$ is shown in comparison with the corresponding no-offset rotation curve. Also shown are the corresponding mass density profiles. The $r_{\text{in}} - \alpha$ plots and histograms for the ISO model are presented in Fig. 16. The ISO simulations are a better (though not perfect) match to the data than the NFW simulations. ISO halos are fairly insensitive to the effects of moderate offsets between optical and dynamical centres. We thus only present the results $\sigma < 2''$.

The peak in the simulated distribution occurs at $\alpha = 0$, offset from the observed $\alpha = -0.2 \pm 0.2$. There is an excess of steeper slope galaxies in the observations. The inner parts of real galaxies clearly have density profiles that are not precisely flat. A possible explanation is that the minimum disk assumption is slightly inappropriate, and that the stellar disk causes the steeper observed slopes. However, as stated before, modeling this effect is beyond the scope of our simple one-component models. The values of the slopes are insensitive to the precise value of the offset, indicating that if galaxies do have ISO halos, they will always be obvious from the observations. The simplest explanation is that offsets between optical and dynamical center are small.

4.6.3 Observational offsets

A mismatch between the centres has the same effect as an incorrectly centered slit. The absence of systematic differences thus also implies an absence of these observational offsets. This is to be expected from technical point of view: the optical centres in LSB galaxies are often visible in the slit camera, and in most cases used to line up the slit of the spectrograph with the galaxy. The accuracy of a typical telescope pointing system and the accuracy of the offset procedure from nearby stars is generally very good. Offset and pointing tests performed during the observations generally are repeatable down to the $\sim 0.3''$ level. This was already addressed by McGaugh, Rubin & de Blok (2001) and dBB02 who present rotation curves of a few LSB galaxies that have been observed multiple times at different dates on different telescopes by different observers and show that these agree very well with each other (see also Marchesini et al. 2002). Residual observational uncertainties could be introduced by the process of measuring the positions of the centres of the galaxies from e.g. CCD images, catalogs or H I observations. These offsets can for obvious reasons only be a small fraction of the size of the galaxy, and are therefore $\sim 1''$ or less, consistent with the scatter implied by the simulations.

5 TESTS WITH REAL DATA

To test whether some of the effects described above are observable in practice, we re-observed one of the galaxies from dBB02. We chose UGC 4325, which is a typical late-type dwarf galaxy. It is nearby ($D = 10.1$ Mpc), resulting in a linear resolution of ~ 50 pc arcsec $^{-1}$. Its H I velocity field is regular, symmetric and appears undisturbed (Swaters 1999) with an inclination of 41° .

UGC 4325 was observed in early Feb 2002 with the 1.93m telescope at the Observatoire de Haute Provence using the long-slit Carelec spectrograph. The set-up, observing procedures and data-reduction were identical to those described in dBB02. We obtained H α spectra of UGC 4325 along its major axis (PA 231°), parallel to the major axis but offset by $+5''$ (0.25 kpc), parallel to the major axis offset by $-5''$, as well as two spectra centered on the galaxy but with position angle offsets of $+30^\circ$ and -30° .

The resulting raw rotation curves (not corrected for inclination) are shown in the top row of Fig. 17. Especially for the offset curves the positions of the ‘‘centres’’ along the slit are difficult to determine, and we determined the systemic velocity and central position by looking for the point that gave maximum symmetry between approaching and receding sides. However, as the curves are almost linearly rising in the inner parts, the precise choice of the centre of symmetry does not affect the slopes. The symmetrized and uncorrected curves are shown in the second row of Fig. 17. Following de Blok, McGaugh & Rubin (2001) we have performed local polynomial fits to the folded curves in order to bring out the underlying shape. We also resampled the curves with a spacing of $4''$. The resulting curves are shown in the third row of Fig. 17. Also shown in the bottom row are the mass-density profiles.

The similarity between the major-axis curve and the two off-axis curves is more consistent with an ISO model

and velocity field as shown in Fig. 3. The curves with position angle offsets only show modest changes in the slope, consistent with U4325 having a fairly axisymmetric potential, and negligible streaming motions. For UGC 4325 the systematic effects discussed in this paper are not obviously present and likely small enough to be unobservable. If UGC 4325 is typical, then the data presented here show that systematic effects discussed in Sect. 3 are unlikely to have a large effect on the observed rotation curves.

6 DISCUSSION

If systematics effects indeed play only a small role in determining the observed mass-density profile, some of the scatter in the observed value of the slope could be due to intrinsic differences in the shapes of the mass-density profiles. This can be used to improve on the results for the ISO halo. Figure 16 shows that for this model the peak in the histogram occurs at values of α that are slightly too large. Here we discuss two additional observationally motivated models that were designed as an improvement on the ISO model. The first one is the Burkert (1995) halo (Sect. 6.1), the second one the halo model proposed by Kravtsov et al. (1998) based on LSB H I rotation curves (Sect. 6.2).

6.1 Burkert halos

The halo model presented in Burkert (1995) is a compromise between the ISO model and CDM models: it has the constant density core found in ISO halos, but shows the steep drop-off in density at large radii found in CDM simulations. The density profile of a Burkert halo can be described as

$$\rho(R) = \frac{\rho_0}{(1 + R/r_0)(1 + (R/r_0)^2)} \quad (11)$$

and the corresponding rotation curve is given by

$$V^2(R) = 2\pi G \rho_0 r_0^3 \frac{1}{R} \left\{ \ln \left[\left(1 + \frac{R}{r_0}\right) \sqrt{1 + \left(\frac{R}{r_0}\right)^2} \right] - \arctan \frac{R}{r_0} \right\}, \quad (12)$$

where r_0 is the equivalent of a core radius and ρ_0 is the central density. This particular model gives a good description of the rotation curves of dwarfs and LSB galaxies (Burkert 1995; Blais-Ouellette et al. 2001; Marchesini et al. 2002). However, the steep R^{-3} drop-off in density in the outer parts, as implied by the above equations, has not been observed unambiguously, and therefore fits using this model mostly constrain the inner part of the curve. Here we characterise the Burkert halo in terms of its maximum rotation velocity, making the assumption that the observed rotation curves do not probe the declining $\rho \sim R^{-3}$ part of the rotation curve. V_{\max} occurs at $R_{\max} = 3.25 r_0$, and we can express r_0 as

$$r_0 = \sqrt{\frac{V_{\max}^2}{0.8606\pi G \rho_0}}. \quad (13)$$

We describe the selection of halo parameters for the simulated Burkert halos in Sec. 6.3.

6.2 Kravtsov et al. (1998) halos

The distribution of observed inner mass-density slopes peaks at a value of $\alpha = -0.2$ (dMBR, dBB02). Before the optical rotation curves used in those analyses became available, Kravtsov et al. (1998) fitted power-law models to the HI rotation curves of dwarfs and LSB galaxies (the latter from de Blok, McGaugh & van der Hulst 1996) and found that the inner rotation curves could be described with a power-law with a slope $\alpha_{\text{HI}} = -0.2$ (the agreement between the optical and HI values is certainly an indication that the effects of beam smearing on the majority of the HI curves must have been minor).

The density profiles described so far are part of a wider set of profiles of the form (Kravtsov et al. 1998; Zhao 1996; Blais-Ouellette et al. 2001)

$$\rho(R) = \frac{\rho_0}{[q + (R/r_0)^{-\alpha}][1 + (R/r_0)^\gamma]^{(\beta+\alpha)/\gamma}} \quad (14)$$

where we have changed the order and signs of some of the exponents as defined in Kravtsov et al. (1998) and Blais-Ouellette et al. (2001) to be consistent with our notation. The above equation can be used to describe NFW halos with $(q, \alpha, \beta, \gamma) = (0, -1, 3, 1)$, ISO halos with $(1, -2, 2, 2)$ while the Burkert halo has parameter set $(1, -1, 3, 2)$. The parameter α determines the inner slope, γ determines the rate of turnover in the mass profile, while β gives the slope of the mass distribution in the outer parts of halos. The q parameter indicates the presence ($q = 1$) or absence ($q = 0$) of a constant-density core. Kravtsov et al. (1998) find that the LSB HI rotation curves from de Blok, McGaugh & van der Hulst (1996) can be best described with the parameter set $(0, -0.2, 3, 1.5)$. They note that the γ and β parameters are difficult to constrain and choose values suggested by CDM simulations. Though we will use these values, we note that the observed mass profiles of LSB galaxies are equally well described by asymptotically flat rotation curves with $\beta = 2$. As we are here only interested in the inner parts of the halos, this choice does not affect the results.

The corresponding rotation curve can be described by a model of the form

$$V(R) = V_t \frac{(R/r_0)^g}{[1 + (R/r_0)^a]^{(g+b)/a}}. \quad (15)$$

The parameter g gives the inner slope of the rotation curve and is related to α by $g = 1 + \alpha/2$ (note our definition as α as a negative number). We thus find $(a, b, g) = (1.5, 0.34, 0.9)$. The maximum rotation velocity is related to V_t by $V_{\text{max}} = V_t(g/a)^{g/a}(1 + g/b)^{-(b+g)/a}$. The parameter sets $(q, \alpha, \beta, \gamma) = (0, -0.2, 3, 2)$ and $(a, b, g) = (1.5, 0.34, 0.9)$ thus fully describe the mass-density profiles and rotation curves of a halo with an $\alpha = -0.2$ inner mass-density profile. These profiles will be used to optimise the description of the data by our simulations.

6.3 Scaling the models

The NFW and ISO models each have a well-defined range of allowed halo parameters, either derived from cosmological simulations or observations. These ranges are less well defined for the Burkert and Kravtsov halos. In order to simulate these halos with realistic parameters we assume that

the ISO curves modeled here are a good description of observed rotation curves. We scale the Burkert and Kravtsov models to show the same diversity in shapes and amplitudes.

The left panel in Fig. 18 compares the rotation curves of each of the three models for $V_\infty = V_{\text{max}} = V_t = 100 \text{ km s}^{-1}$, and $R_C = r_0 = 1 \text{ kpc}$. Using these identical numerical parameters the ISO curve rises more slowly than the Burkert and Kravtsov curves. The latter has a lower maximum velocity, as for this model $V_{\text{max}} = 0.62 V_t$ (see Sec. 6.2). Simply using identical halo parameters in the simulations thus makes the Burkert and Kravtsov halos consistently more compact and more likely to suffer from systematic resolution effects. The differences in Fig. 18 are due to the different scalings that r_0 and R_C imply in the various models and we can scale the curves in order to get a more consistent behaviour. Equations 10 and 13 show that for a given central density and maximum or asymptotic velocity, the ISO and Burkert radii scale as $R_C/r_0 = 1/2.156$. For a given central density and maximum velocity, one needs to assume a value of r_0 that is ~ 2.2 times larger than the corresponding value of R_C in order to get a Burkert curve that matches approximately the shape of the ISO curve. The Burkert and Kravtsov curves can be scaled in radius by considering their maximum rotation velocities. For the Burkert halo this occurs at $r = 3.25 r_0$; for the Kravtsov halo at $r = 1.91 r_0$. A scaling of 1.69 in radius will thus line up the Kravtsov curve with the Burkert one (which implies a total scaling of 3.64 with respect to the ISO halo).

The velocity scales can be matched with those of the ISO halos by multiplying the velocities of the Burkert halo with 0.86; that of the Kravtsov halo by multiplying with 1.38. We do not normalise to the asymptotic velocity of the ISO halo as might perhaps be expected, as this would have resulted in substantially different shapes. The right panel in Fig. 18 shows the scaled rotation curves. This procedure thus merely serves to get a sample of simulated Burkert and Kravtsov curves with shapes that match those shown by the ISO curves (and as observed in real galaxies). This minimises possible systematic effects in the simulations due to differences in shape or resolution. The scaling does not affect the values of the central slopes.

In order to simulate a realistic range of parameters for the Burkert and Kravtsov halos we sample the same numerical range of parameters as for the ISO halos (as described in Sect. 3.2.2), and multiply their radial and velocity scales by the factors described above.

6.4 Results for Burkert and Kravtsov halos

As we established that the systematic effects for core-dominated models can only be small, we concentrate here on the simulation results in the absence of these effects, except for the small $\sigma = 0.5''$ scatter in the position of the dynamical centre (see Sect. 4.6.2). Results for the Burkert halos are expected to be similar to those of the ISO model, as the Burkert model was designed to be a compromise between a core model in the inner parts and a CDM $\rho \sim R^{-3}$ model in the outer parts. As is clear from Fig. 19, the only real difference is that the Burkert models show a slightly larger number of steep slopes than the ISO model, due to the steeper drop-off in the outer parts.

Fig. 20 shows the results for the Kravtsov halos. The

peak of the histogram distribution now matches well (but was constructed to do so). The $r_{\text{in}} - \alpha$ distributions show slopes that are slightly too shallow for large values of r_{in} . This is introduced by the rotation curve scaling we used and the points can be shifted horizontally by using a different scaling. However, as we are only interested in the global trends, and are not trying to model individual galaxies in detail, we retain our simple scaling relations. The scaling does not affect the inner slopes.

We show the velocity field of a Kravtsov halo in Fig. 21. The halo parameters were chosen to give a rotation curve similar to the one used for the ISO velocity field in Fig. 3. The shape of the iso-velocity contours is very similar to the ISO velocity field, and do not show the “pinching” that the NFW iso-velocity contours show.

6.5 Kravtsov halos with scatter

The Kravtsov model fits the peak in the α histogram best, but was of course constructed to do so. One feature of the data that none of the three core-dominated models can reproduce are the wings towards steeper slopes found in the data histogram. It is easy to produce shallower slopes with systematic effects, but very few effects actually will produce steeper slopes. Furthermore, the “monolithic” nature of the models (for each model all halos have identical slopes) creates pronounced peaks in the histograms. In real galaxies we might expect the contributions of e.g. the disk to differ from galaxy to galaxy, introducing a scatter in the values for the inner total mass-density slope. We test here the hypothesis that there is a small scatter in the intrinsic value of the inner slopes which is responsible for the observed wings in the data histograms.

We use the Kravtsov model and add a small Gaussian scatter to the slope. We choose an intrinsic dispersion in the mass-density slope $\sigma_\alpha = 0.2$. This choice has no physical motivation, but is simply suggested by the width of the peak in the data histogram. Other more fine-tuned choices may very well be possible, our aim here is simply to describe the data in as few assumptions as possible with a simple one-component model. Adding a Gaussian scatter σ_α to the α -parameter in Eq. 14, implies modifying the g -parameter in Eq. 15 with a Gaussian contribution with dispersion $\sigma_g = \sigma_\alpha/2$.

The results for the Kravtsov simulations with scatter $\sigma_\alpha = 0.2$ are shown in Fig. 22. The peak again matches (naturally). The high- and low- α wings of the histogram fit the data better than previous models. The value for the scatter can probably be fine-tuned, and the distribution of the scatter is most likely not Gaussian (our assumptions in a small number of cases lead to hollow halos). The observed distributions of slopes is thus consistent with halos with inner slopes $\alpha = -0.2 \pm 0.2(1\sigma)$ and no systematic effects.

7 CONCLUSIONS

We have investigated the effect of systematic effects such as non-circular motions, asymmetries and lopsidedness on the values of the inner slopes of various halo models. We find that no realistic combination of a single systematic effect

and NFW models can explain the observed distribution of slopes.

Core-dominated models, on the other hand, are consistent with the data in the absence of large systematic effects. The best match to the data is obtained by using halos with an inner mass-density slope $\alpha = -0.2$ and an intrinsic Gaussian scatter in the slope of $\sigma_\alpha \sim 0.2$. As our models assume minimum disk, these slopes should be interpreted as those of the combined mass-profiles of stars, gas and dark matter in a galaxy.

It is perhaps possible to construct a combination of multiple systematic effects to explain the data in the CDM framework. However, such a combination of effects would have to completely wipe out the strong $\alpha = -1$ peak in the α histograms. The resulting models would be completely dominated by non-cosmological effects, and not contain any link between properties of dark matter halos and the visible galaxies that inhabit them. Yet, they would have to explain and obey the Tully-Fisher relation, for example, and thus require a tremendous amount of fine-tuning.

The implied observational signature of CDM halos is strong and if present should be easily seen.

We thus conclude that the trends observed in the $r_{\text{in}} - \alpha$ plot are mostly resolution effects, in combination with intrinsic scatter in the inner slopes. The cusp problem is certainly genuine; it can not plausibly be attributed to systematic errors in the data. LSB galaxies have shallow mass-density slopes implying that (i) the current CDM model, or more precisely the current generation of N-body models based on the CDM prescription, do not correctly describe structure at the scale of galaxies, or (ii) non-cosmological effects destroy the cusp. The second option reduces the elegance and predictive power of the CDM model.

ACKNOWLEDGEMENTS

EdB thanks PPARC for Advanced Fellowship support.

REFERENCES

- Adler, D.S., Westpfahl, D.J., 1996, AJ, 111, 735
- Athanassoula, L., 2002, ApJ, 569, L83
- Begeman, K.G., 1987, PhD Thesis, University of Groningen
- Blais-Ouellette, S., Amram, P., Carignan, C., ApJ, 121, 1952
- Bosma, A., 1978, PhD thesis, University of Groningen
- Bosma, A., Byun, Y.I., Freeman, K.C., & Athanassoula, E., 1992, ApJL, 400, L23
- Bullock, J.S., Kolatt, T.S., Sigad, Y., Somerville, R.S., Kravtsov, A.V., Klypin, A.A., Primack, J.R., & Dekel, A. 2001, MNRAS, 321, 559
- Burkert, A., 1995, ApJ, 447, L25
- de Blok, W.J.G., McGaugh, S.S., 1997, MNRAS, 290, 533
- de Blok, W.J.G., Bosma, A., 2002, A&A, 385, 816
- de Blok W.J.G., McGaugh S.S., van der Hulst J.M., 1996, MNRAS, 283, 18
- de Blok, W.J.G., McGaugh, S.S., Rubin, V.C., 2001, AJ, 122, 2396
- de Blok, W.J.G., van der Hulst, J.M., Bothun, G.D., 1995, MNRAS, 274, 235

- de Blok, W.J.G., McGaugh, S.S., Rubin, V.C., Bosma, A., 2001, *ApJ*, 552, L23
- de Vaucouleurs, G., Freeman, K.C., 1972, *Vistas in Astronomy*, 14, 163
- Deul, E.R., van der Hulst, J.M., 1987, *A&A Sup.*, 67, 509
- Dubinski, J., & Carlberg, R.G., 1991, *ApJ*, 378, 495
- Firmani, C., D'Onghia, E., Avila-Reese, V., Chincarini, G., Hernández, X., 2000, *MNRAS*, 315, L29
- Flores, R.A., Primack, J.R., 1994, *ApJL*, 427, L1
- Garrido, O., Marcelin, M., Amram, P., Boulesteix, J., 2002, *A&A*, 387, 821
- Jörsäter, S., van Moorsel, G.A., 1995, *AJ*, 110, 2037
- Kravtsov, A.V., Klypin, A.A., Bullock, J.S., & Primack, J.R., 1998, *ApJ*, 502, 48
- Marchesini, D., D'Onghia, E., Chincarini, G., Firmani, C., Conconi, P., Molinari, E., Zacchei, A., 2002, *ApJ*, 575, 801
- Matthews, L.D., Wood, K., 2001, *ApJ*, 548, 150
- McGaugh, S.S., de Blok, W.J.G., 1998, *ApJ*, 499, 41
- McGaugh, S.S., Barker, M.K., de Blok, W.J.G., 2003, *AJ*, in press (astro-ph/0210641)
- McGaugh, S.S., Rubin, V.C., de Blok, W.J.G., 2001, *AJ*, 122, 2381
- Moore, B. 1994, *Nature*, 370, 629
- Moore, B., Governato, F., Quinn, T., Stadel, J., Lake, G., 1998, *ApJL*, 499, L5
- Moore, B., Quinn, T., Governato, F., Stadel, J., Lake, G., 1999, *MNRAS*, 310, 1147
- Navarro, J.F., Frenk, C.S., White, S.D.M. 1996, *ApJ*, 462, 563
- Navarro, J.F., Frenk, C.S., & White, S.D.M. 1997, *ApJ*, 490, 493
- Pisano, D.J., Wilcots, E.M, Elmegreen, B.G, 1998, *AJ*, 115, 975
- Puche, D., Carignan, C., Bosma, A., 1990, *AJ*, 100, 1468
- Sackett, P.D., 1997, *PASA*, 14, 11
- Salucci, P., 2001, *MNRAS*, 320, L1
- Salucci, P., Borriello, A., 2001, *MNRAS*, 323, 285
- Swaters, R.A., 1999, PhD Thesis, University of Groningen
- Swaters, R.A., Madore, B.F., Trewhella, M., 2000, *ApJL*, 531, L107
- Swaters, R.A., Schoenmakers, R.H.M., Sancisi, R., van Albada, T.S., 1999, *MNRAS*, 304, 330
- Swaters, R.A., Madore, B.F., van den Bosch, F.C., Balcells, M., 2002, *ApJ*, in press (astro-ph/0210152)
- van den Bosch, F.C., Swaters, R.A., 2001, *MNRAS*, 325, 1017
- Wechsler, R.H., Bullock, J.S., Primack, J.R., Kravtsov, A.V., Dekel, A., 2002, *ApJ*, 568, 52
- Weldrake, D.T.F., de Blok, W.J.G., Walter, F., *MNRAS*, in press (astro-ph/0210568)
- Zhao, H.S., 1996, *MNRAS*, 278, 488

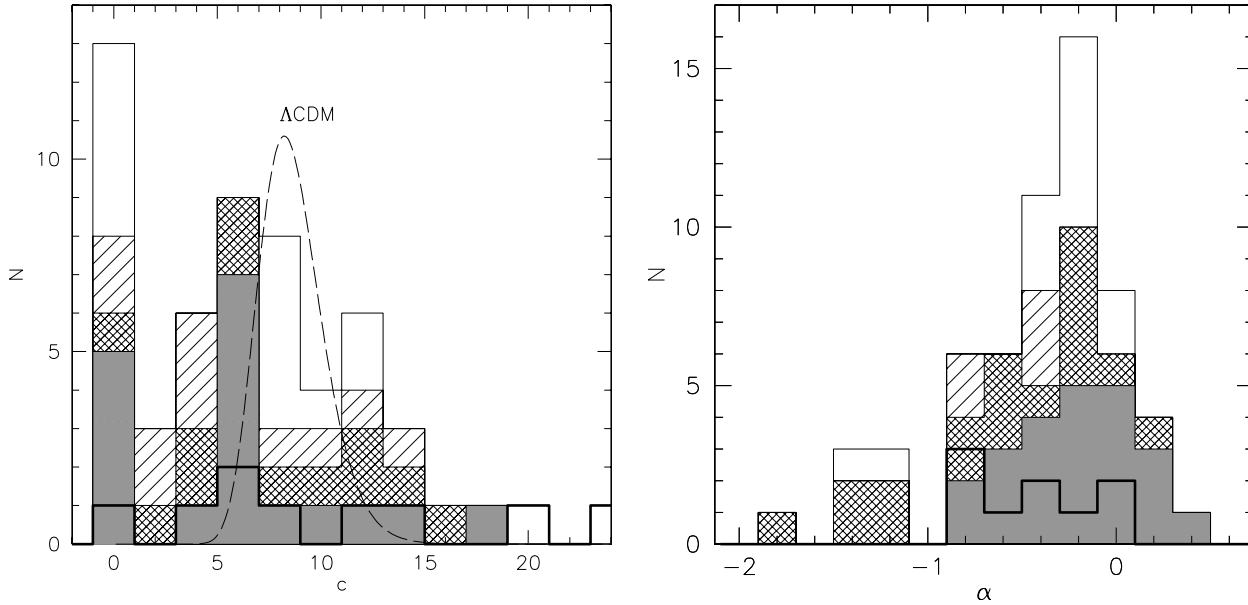


Figure 1. Distribution of the NFW concentration parameter c (left panel) and the inner mass-density slope α (right panel) based on the data from dBMBR and dBB02. The various superimposed histograms show the different stages of pruning: open histogram: full sample from dBB02 and dBMBR; single hatched histogram: galaxies with $i < 30^\circ$ and $> 85^\circ$ have been removed; double hatched histogram: galaxies with low-quality rotation curves, asymmetries etc. have been removed; grey filled histogram: galaxies with less than 2 independent data points in the inner 1 kpc are removed. The thick open histogram in shows the restricted SMBB sample. The dashed curve in the left panel shows the expected distribution of c for a Λ CDM universe (e.g. McGaugh, Barker & de Blok 2003; Bullock et al. 2001).

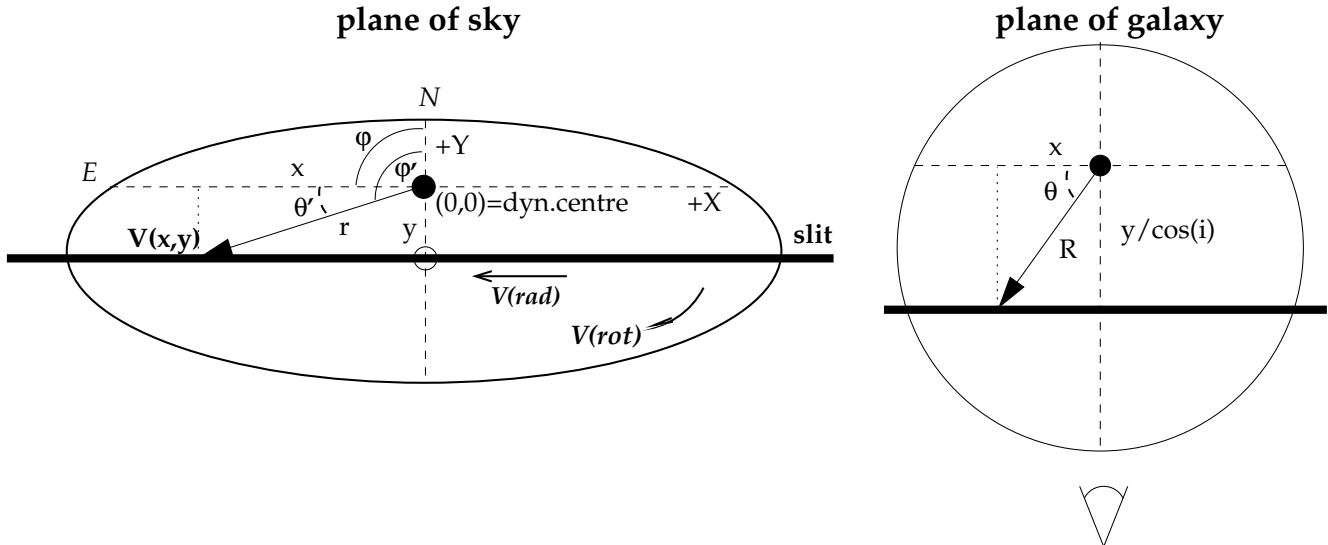


Figure 2. Sketch of the geometry of an inclined rotating disk projected on the sky. All angles and distances are measured in the plane of the sky, except R and θ which are measured in the plane of the galaxy. See text for more details.

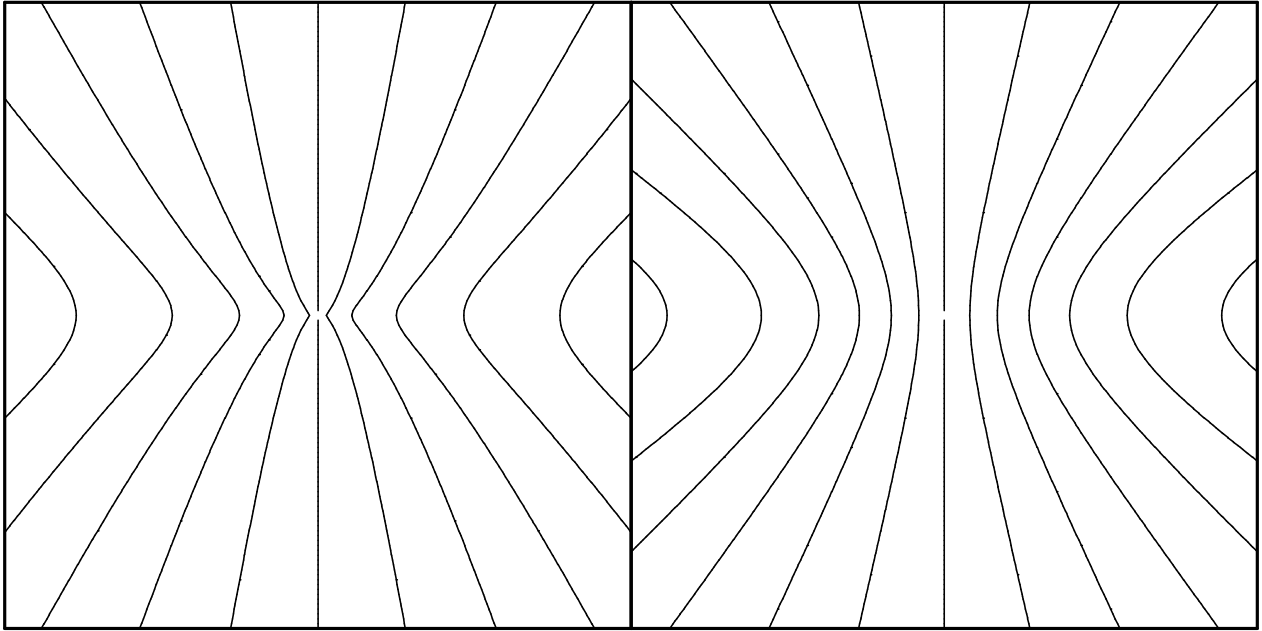


Figure 3. Velocity fields of the inner parts of massless disks embedded in a NFW halo (left panel) and an ISO halo (right panel). The velocity field is seen under an inclination angle of 60° , and a position angle of 90° . The boxes measure 5×5 kpc. The vertical minor axis contour is 0 km s^{-1} , increasing in steps of 10 km s^{-1} outwards. The NFW halo parameters are $c = 8.6$ and $V_{200} = 100 \text{ km s}^{-1}$, the ISO parameters are $R_C = 1 \text{ kpc}$ and $V_\infty = 100 \text{ km s}^{-1}$.

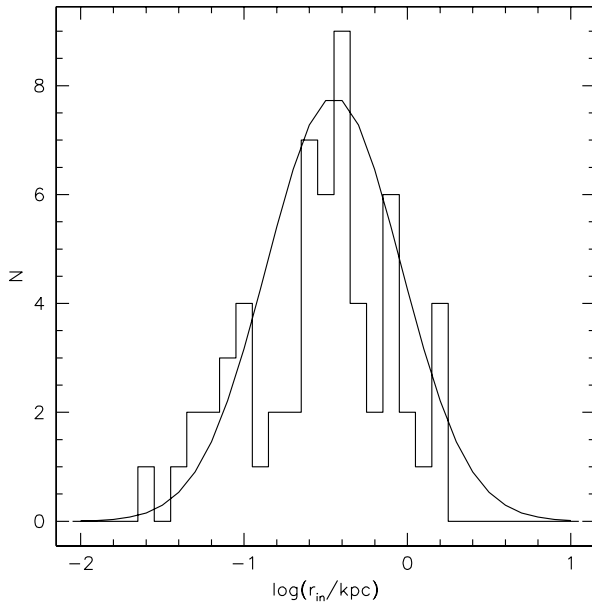


Figure 4. Distribution of the resolutions $\log r_{\text{in}}$ of the rotation curves in presented in dBMBR and dBB02. Over-plotted is a Gaussian with average $\mu(\log r_{\text{in}}) = -0.45$ and $\sigma(\log r_{\text{in}}) = 0.41$ which was used as probability distribution for the simulations.

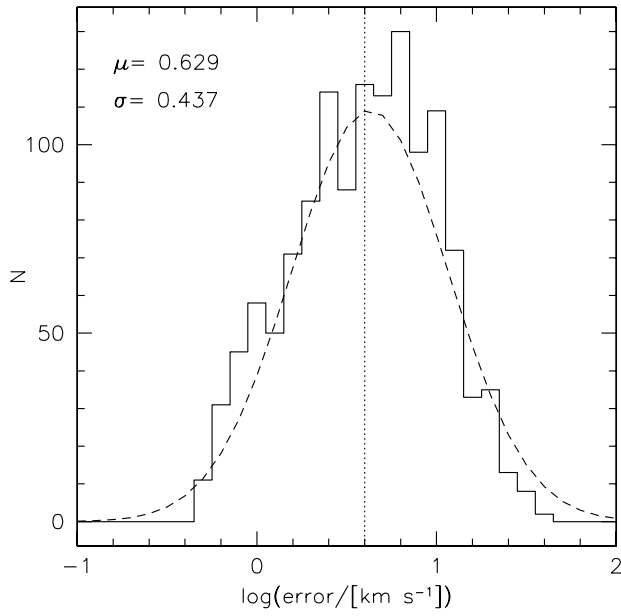


Figure 5. Distribution of the error-bars in the unsmoothed rotation curves presented in dBB02. Over-plotted is a best fitting Gaussian with $\mu = 0.629$ and $\sigma = 0.437$. This was used as the probability distribution for assigning error s . The vertical line indicates the value of 4 km s^{-1} . Errors smaller than 4 km s^{-1} , were set to be 4 km s^{-1} , in a similar way as the data.

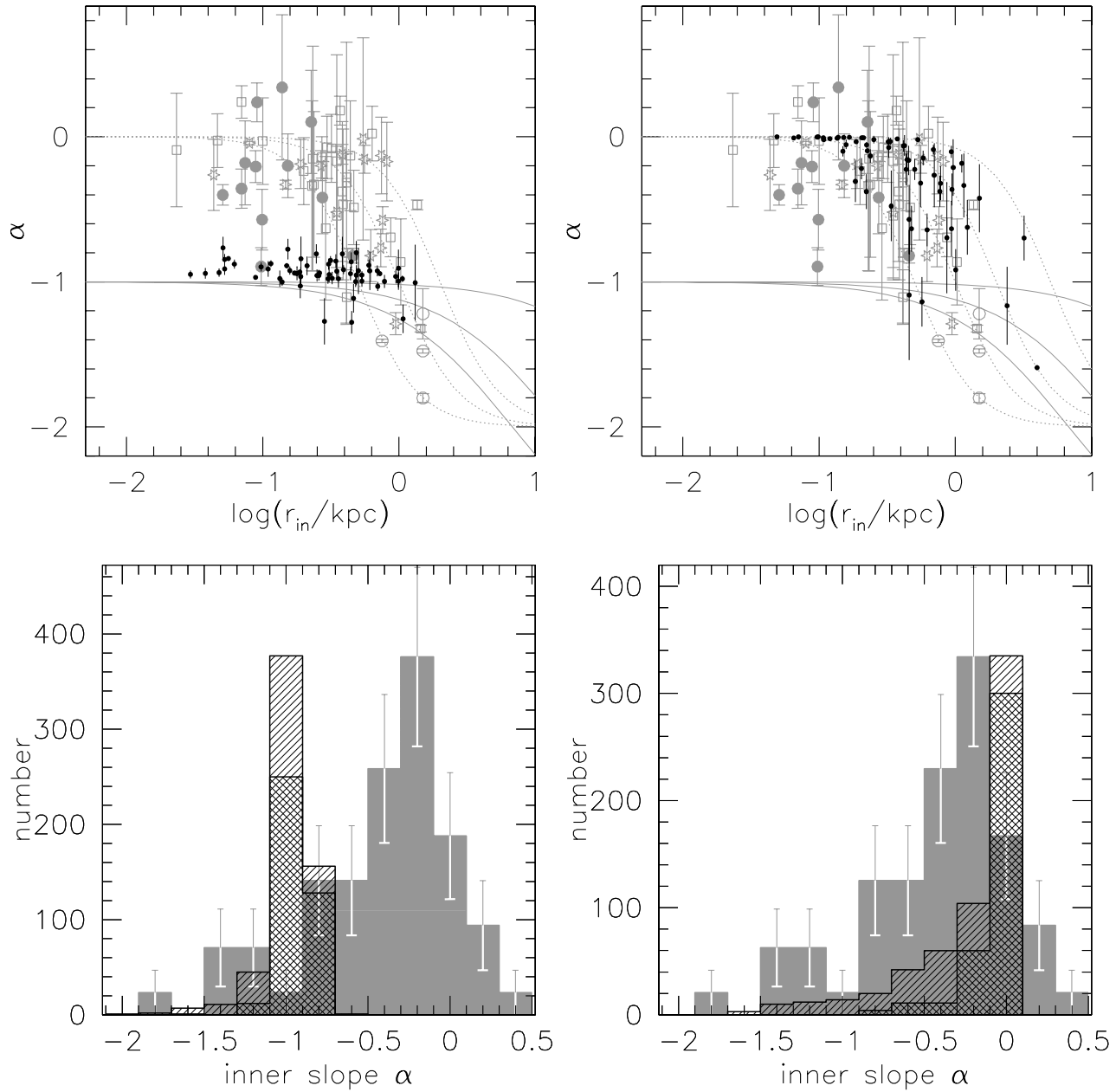


Figure 6. Comparison of the simulated NFW (left) and ISO (right) halos. The top row shows compares the simulated $r_{\text{in}} - \alpha$ data points (black) with the observed distribution from dBMBR and dBBO2 (grey data points). No systematic effects are assumed. The grey dotted lines converging on $\alpha = 0$ represent the theoretical variations in slope for ISO halos with $R_C = 0.5, 1, 2$ kpc. The lines converging on $\alpha = -1$ show the variation in slope for $c/V_{200} = 9.8/50, 8.6/100, 6.1/500$ (the slope only depends on the ratio c/V_{200}). The bottom row shows the histograms of α values for the two models. The double hatched histogram indicates well-resolved galaxies with $r_{\text{in}} \leq 0.5$ kpc.

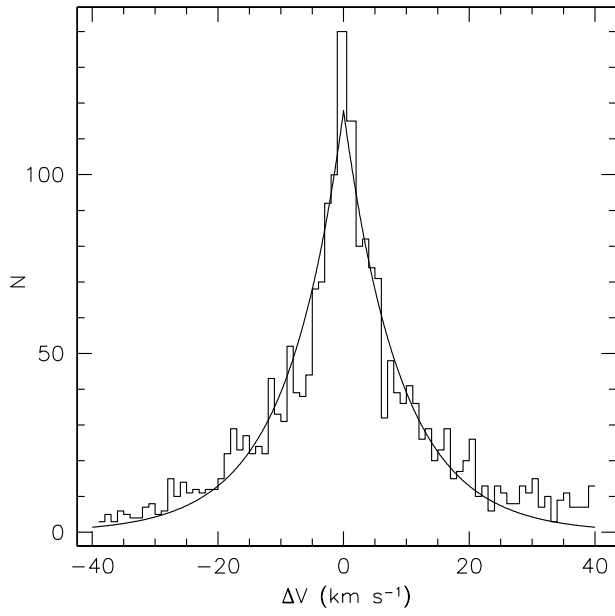


Figure 7. Histogram of the deviations of the raw data points from the underlying smooth rotation curves presented in de Blok, McGaugh & Rubin (2001). The distribution is symmetrical, and can be well described by a function of the form $N = 117.9 e^{-|\Delta V|/9.06}$, as shown by the superimposed curve.

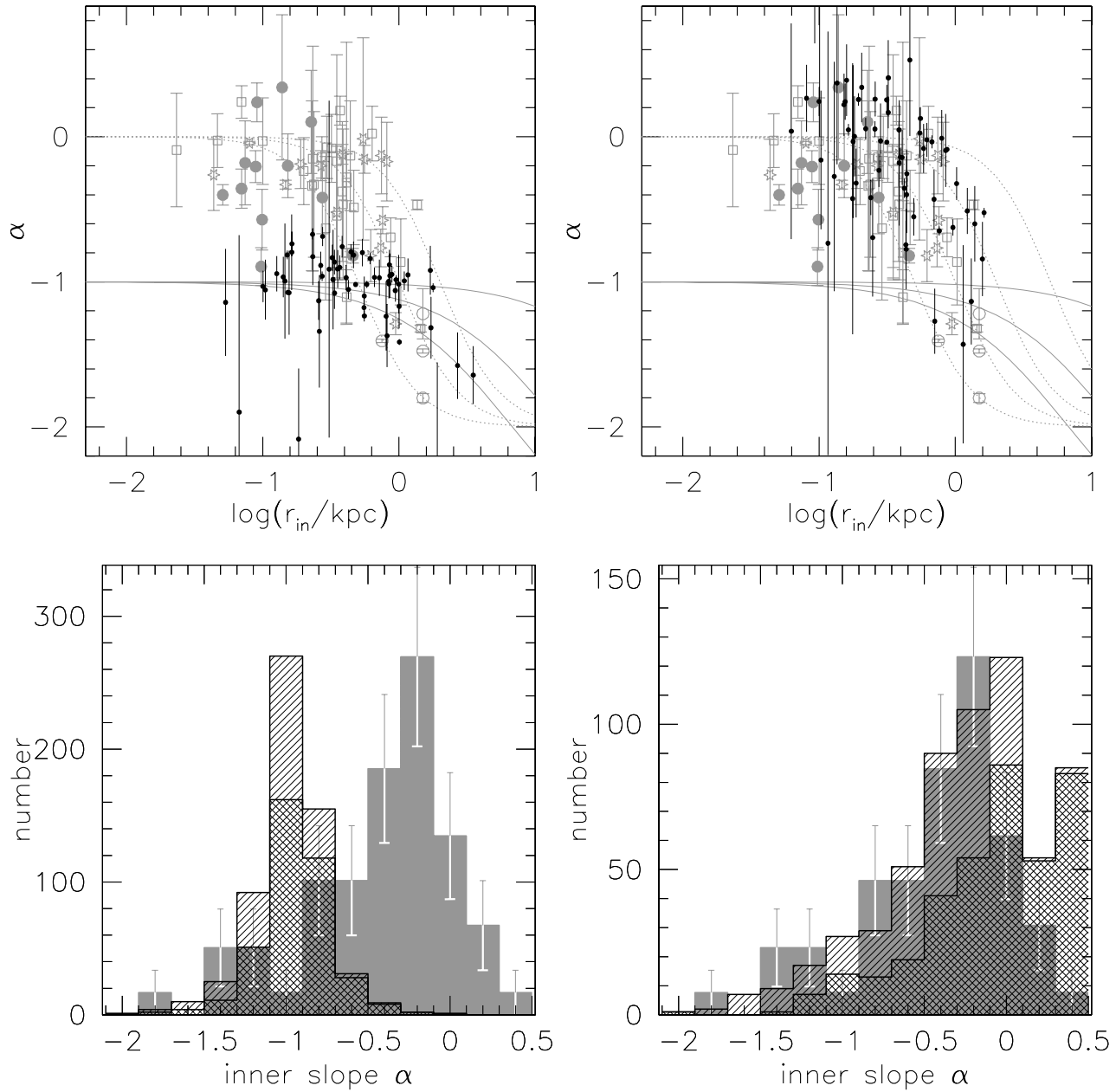


Figure 8. Comparison of the simulated NFW (left column) and ISO (right column) halos with rotation curves modified by small-scale velocity deviations. The top row compares $r_{\text{in}} - \alpha$ data points with the observed distribution. The bottom row shows the histograms of α values for the two models. Apart from extra scatter, the addition of small-scale deviations has not changed the general trend. See Fig. 6.

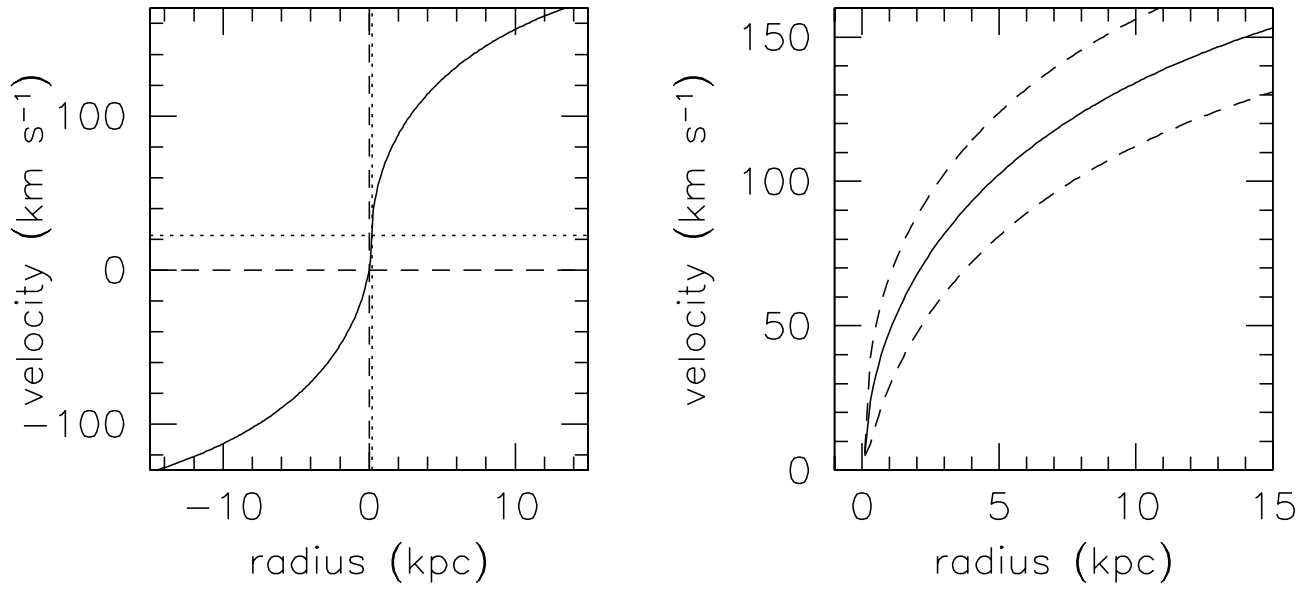


Figure 9. Example of the construction of a lopsided rotation curve. The left panel shows a symmetric NFW halo rotation curve. The dotted lines indicate the true point of symmetry. The dashed lines indicate the “wrong” centre of symmetry used to construct the lopsided curve. The offset is 0.2 kpc in radius and 22 km s⁻¹ in velocity. The right panel shows the lopsided curve (drawn line) which is the average of the approaching and receding sides’ curves (dashed lines).

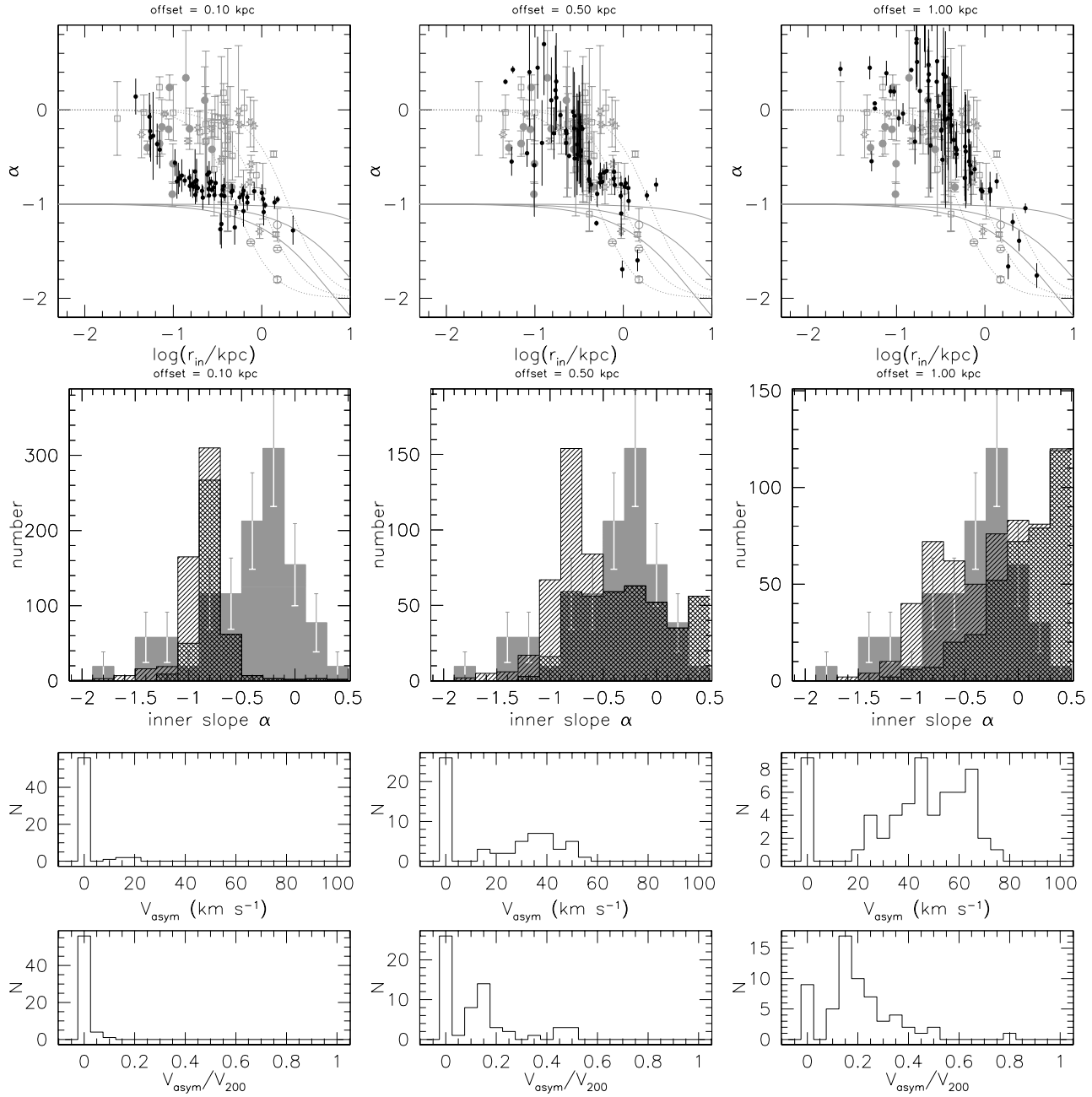


Figure 10. As Fig. 6, but now showing the results for NFW halos in combination with kinematical lopsidedness of 0.1 kpc (left column), 0.5 kpc (centre column) and 1 kpc (right column). The bin at $\alpha = 0.5$ also contains galaxies with $\alpha > 0.5$. The bottom rows shows the distribution of the resulting velocity differences between approaching and receding sides, both in absolute terms, and as a fraction of halo rotation velocity V_{200} . The peak at $V = 0$ is due to galaxies at large distance or low inclinations where the kinematical lopsidedness shift is much less than one resolution element.

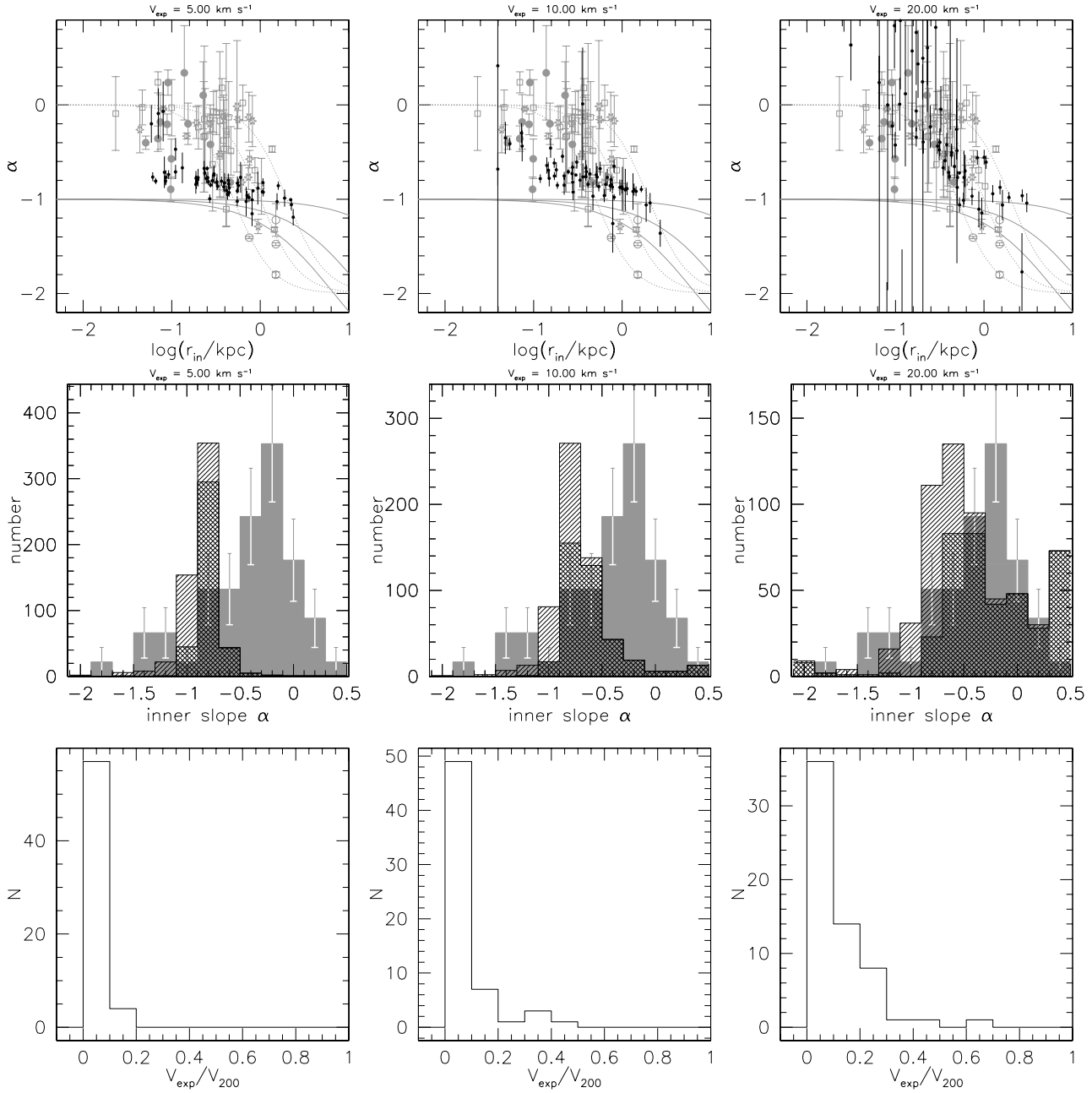


Figure 11. As Fig. 6, but now showing the results for NFW halos in combination with streaming motions parallel to the minor axis. The left panel shows results for 5 km s^{-1} , centre for 10 km s^{-1} and right panels for 20 km s^{-1} . The bin at $\alpha = 0.5$ also contains galaxies with $\alpha > 0.5$. The bottom row shows the distribution of the magnitude of the streaming motion as a fraction of the halo velocity V_{200} .

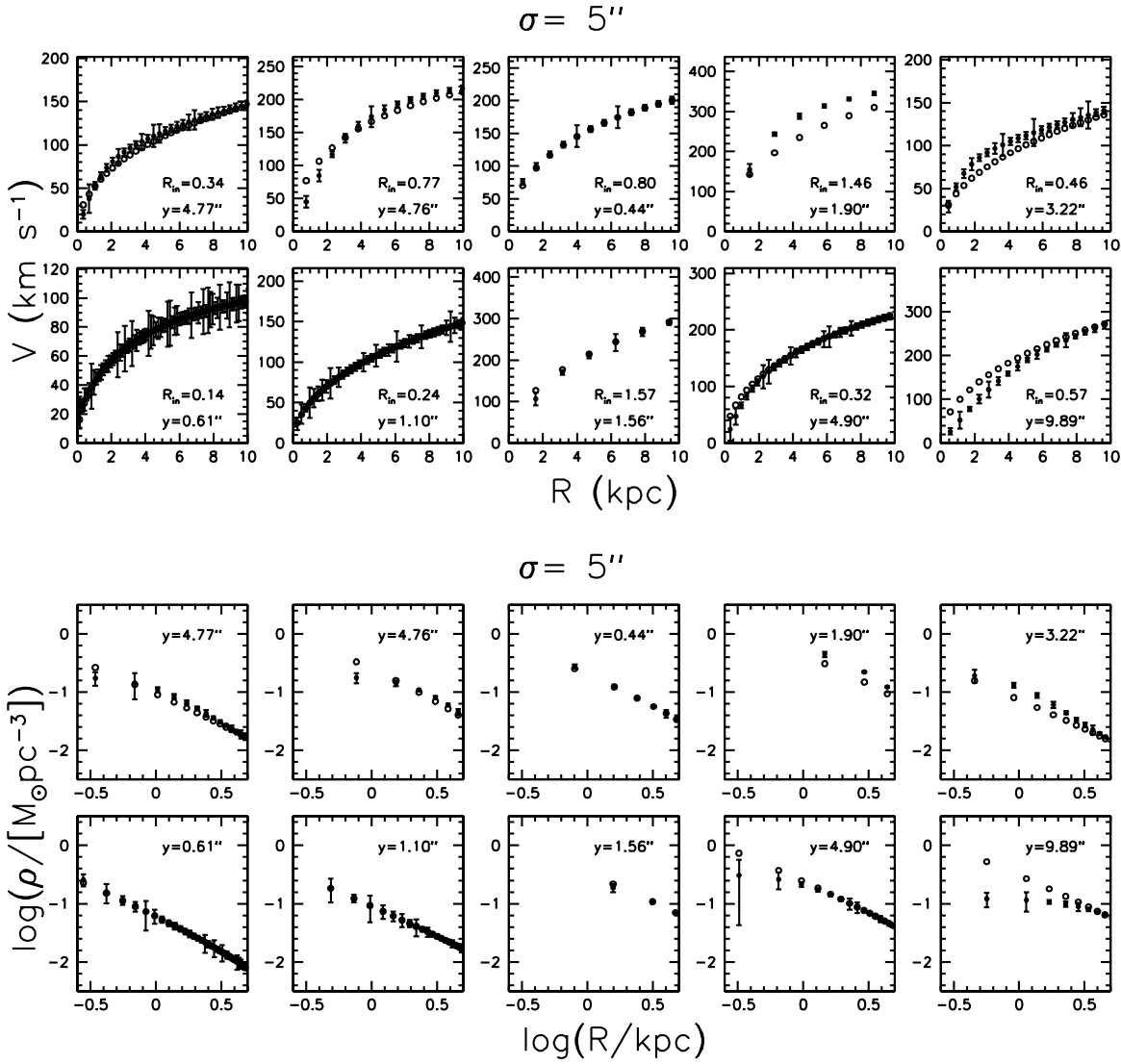


Figure 12. A random selection of simulated NFW rotation curves (top panel) and corresponding density profiles (bottom panel). The open circles show the original major axis curves and profiles, while the filled circles with error-bars show the off-axis curves and profiles. A Gaussian scatter with $\sigma = 5''$ was used for these curves. The actual value is given in the sub-panels, along with the resolution (separation between points) in kpc.

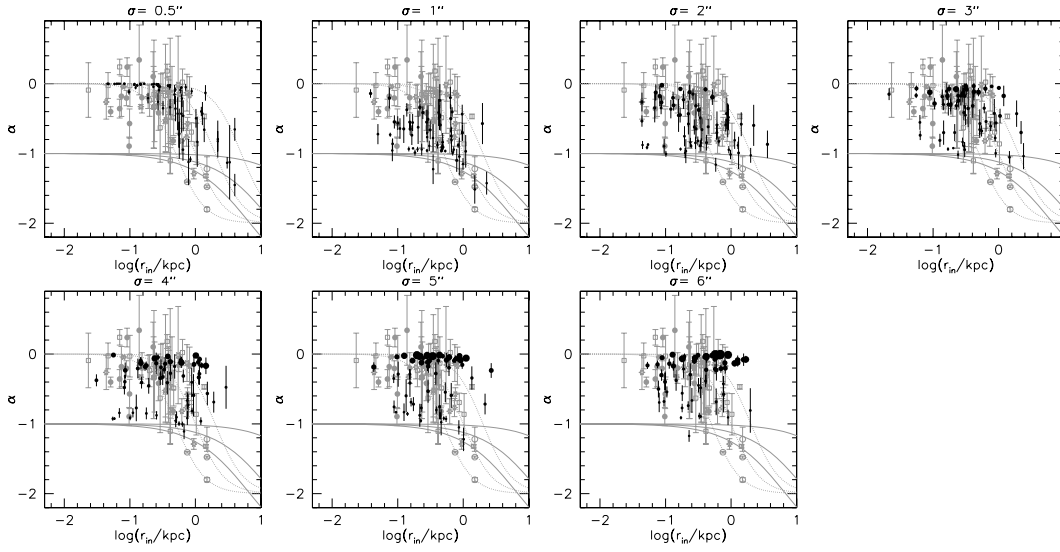


Figure 13. Comparison of the simulated NFW halo $r_{in} - \alpha$ data points with the observed distribution. The simulated data points were derived using random centre offsets, where the offsets have a Gaussian distribution with the dispersion given above each sub-panel. As Fig. 6.

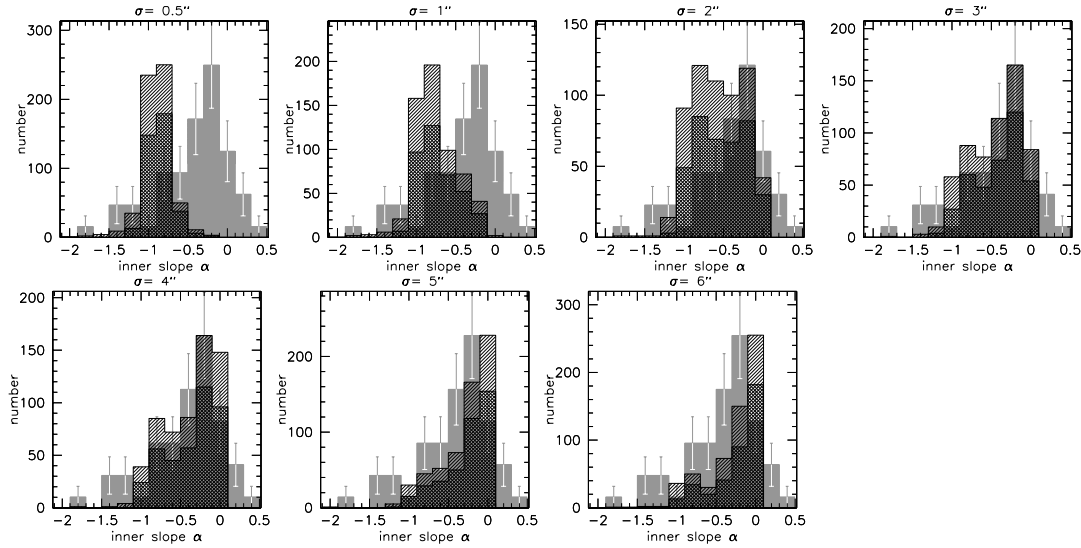


Figure 14. Comparison of the simulated distribution of NFW halos slopes (hatched histogram; low-resolution galaxies: single-hatched; high-resolution galaxies: cross-hatched) with that actually observed (grey histogram). The dispersion of the Gaussian distribution for offsets is given above each sub-panel.

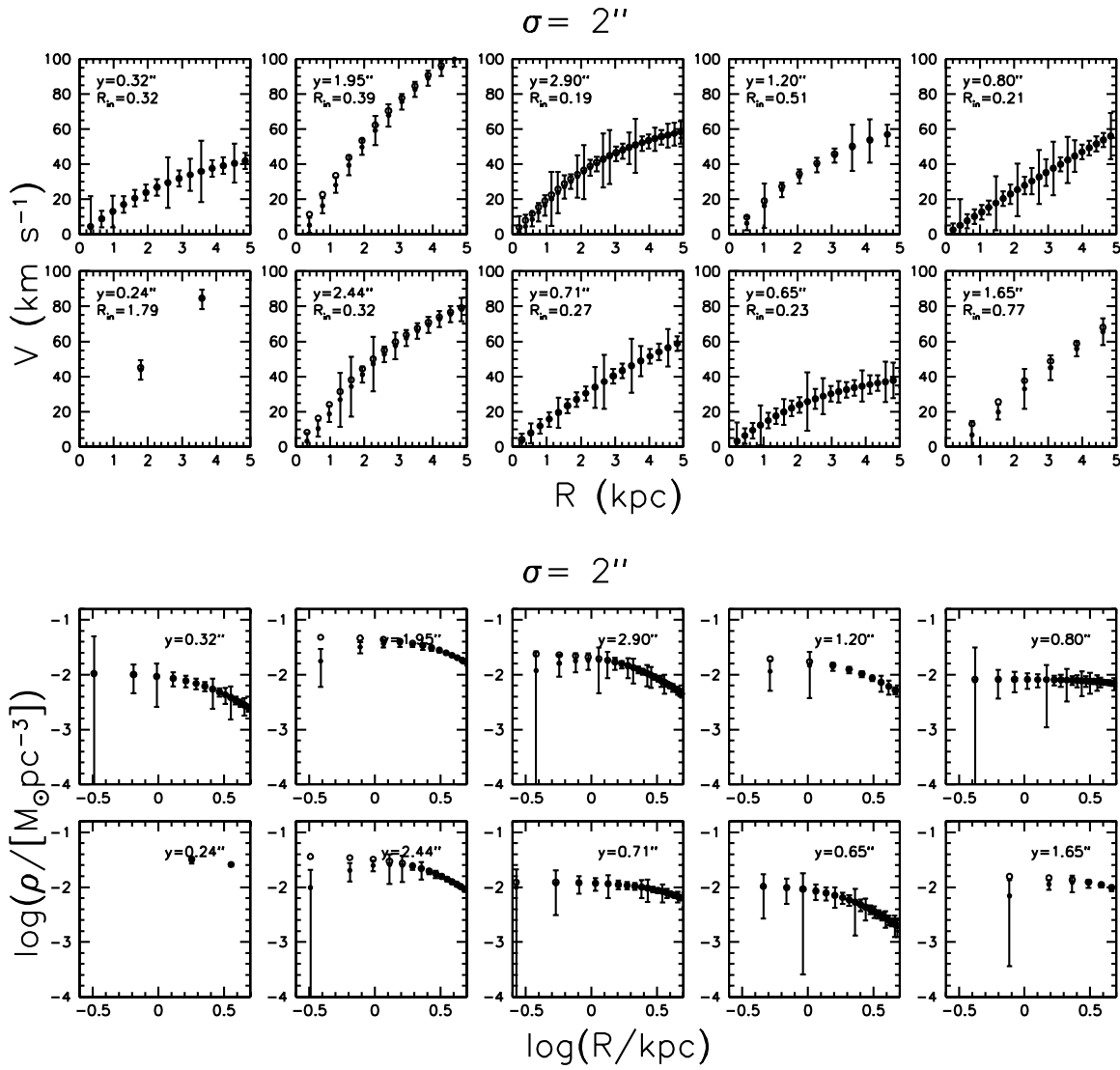


Figure 15. As Fig. 12, but showing ISO curves and profiles.

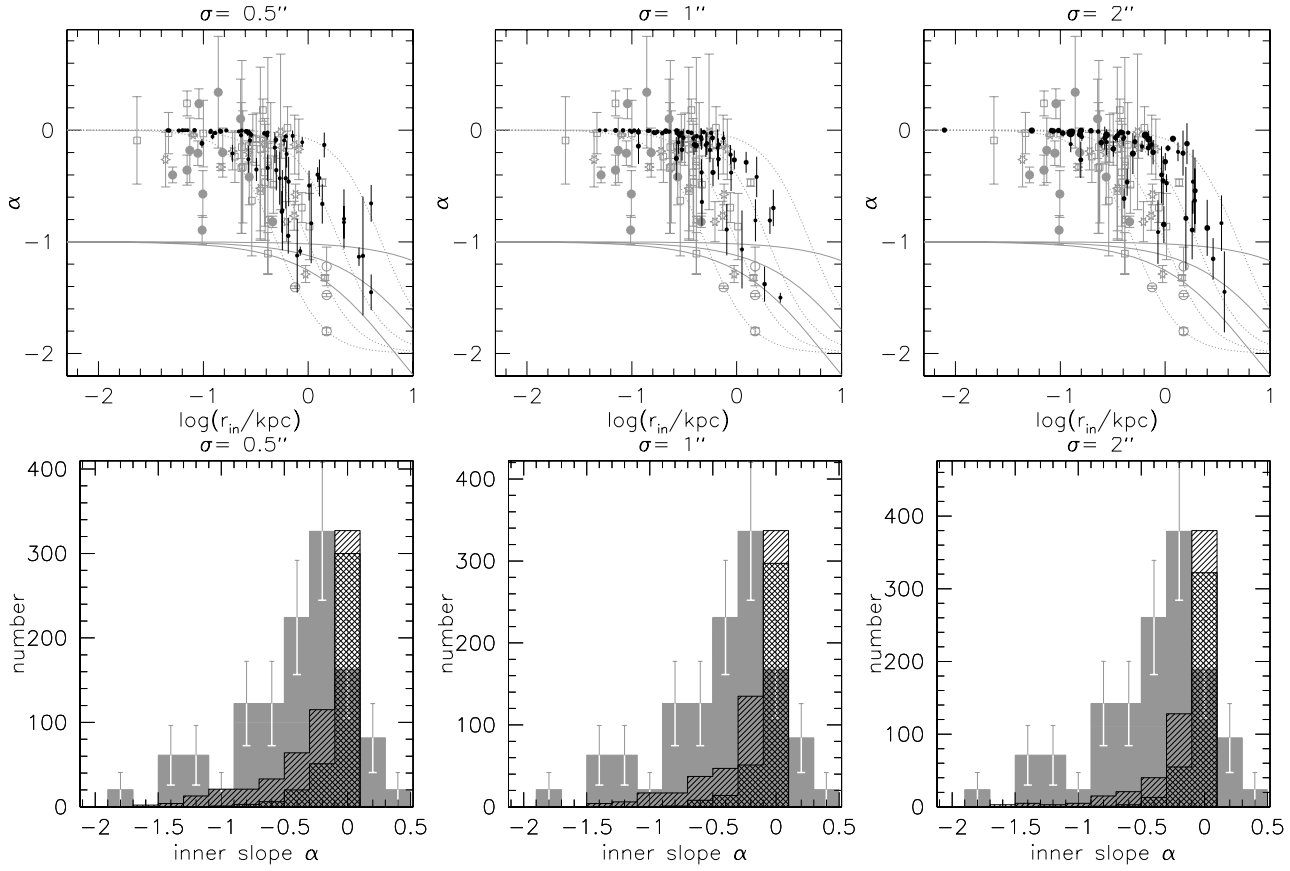


Figure 16. As Figs. 13 and 14, but now showing the results for ISO halos. The bin at $\alpha = 0.5$ also contains galaxies with $\alpha > 0.5$.

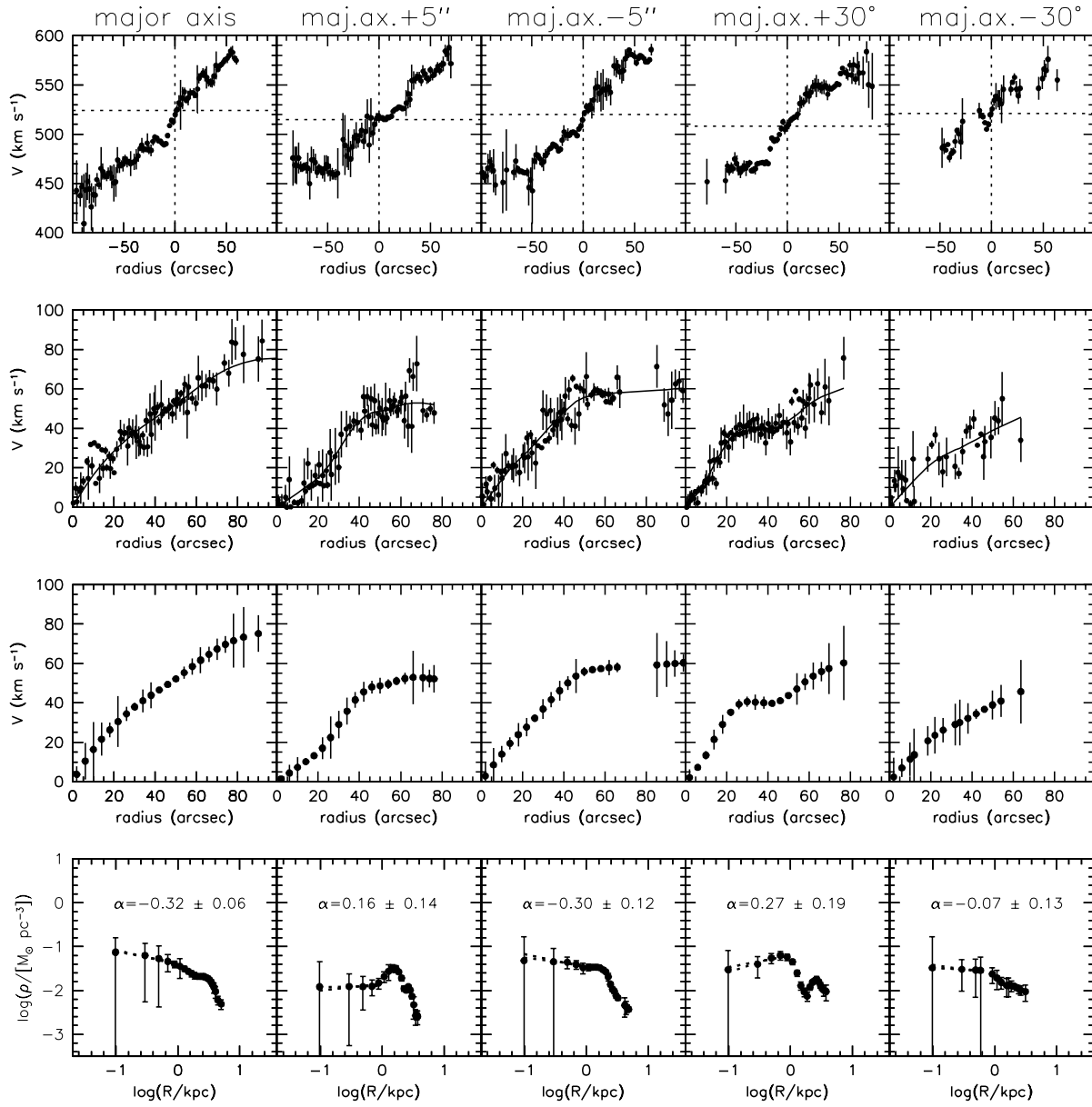


Figure 17. Observed rotation curves of UGC 4325, after applying spatial and position angle offsets. From left to right: major axis rotation curve; parallel to major axis offset by +5''; parallel to major axis offset by -5''; position angle offset of +30°; position angle offset of -30°. Top row shows the raw rotation curves. Second row shows folded rotation curves. Third row shows re-sampled rotation curves. Bottom row shows mass-density profiles derived from the re-sampled rotation curves.

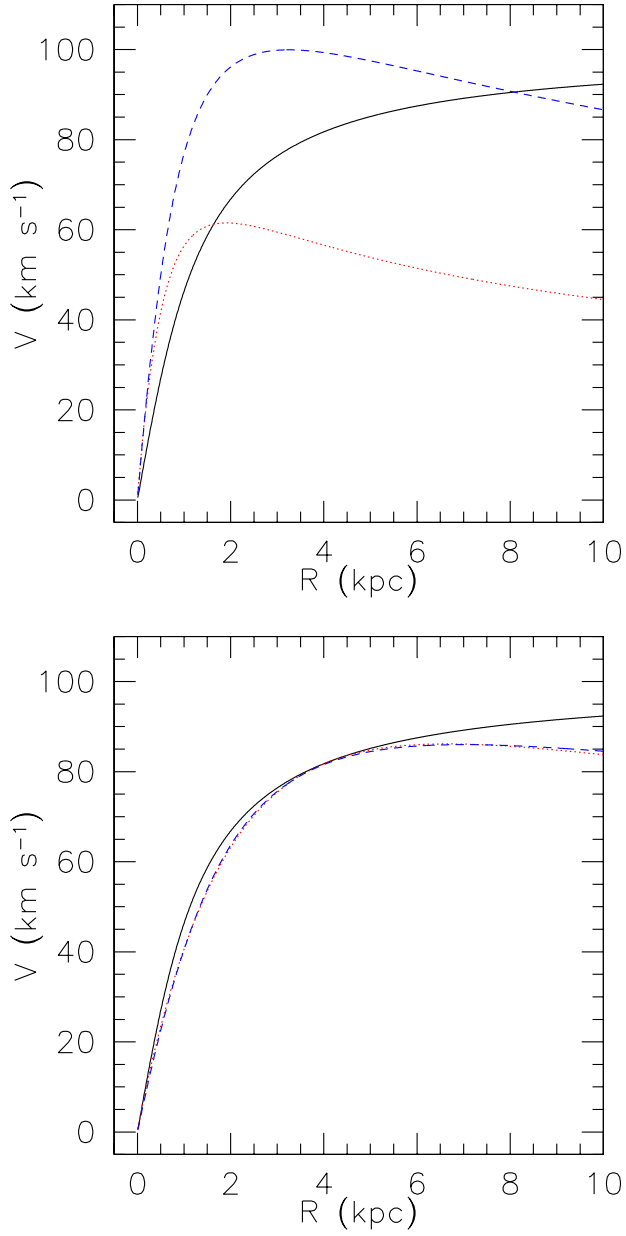


Figure 18. Comparison of the rotation curves of the ISO, Burkert and Kravtsov models, before and after scaling. Left panel: rotation curves of the three models, assuming $V_\infty = V_{\text{max}} = 100 \text{ km s}^{-1}$, and $R_C = r_0 = 1 \text{ kpc}$. Full drawn curve: ISO halo; dotted curve: Kravtsov halo; dashed curve: Burkert halo. Right panel: the three curves after the scaling described in the text.

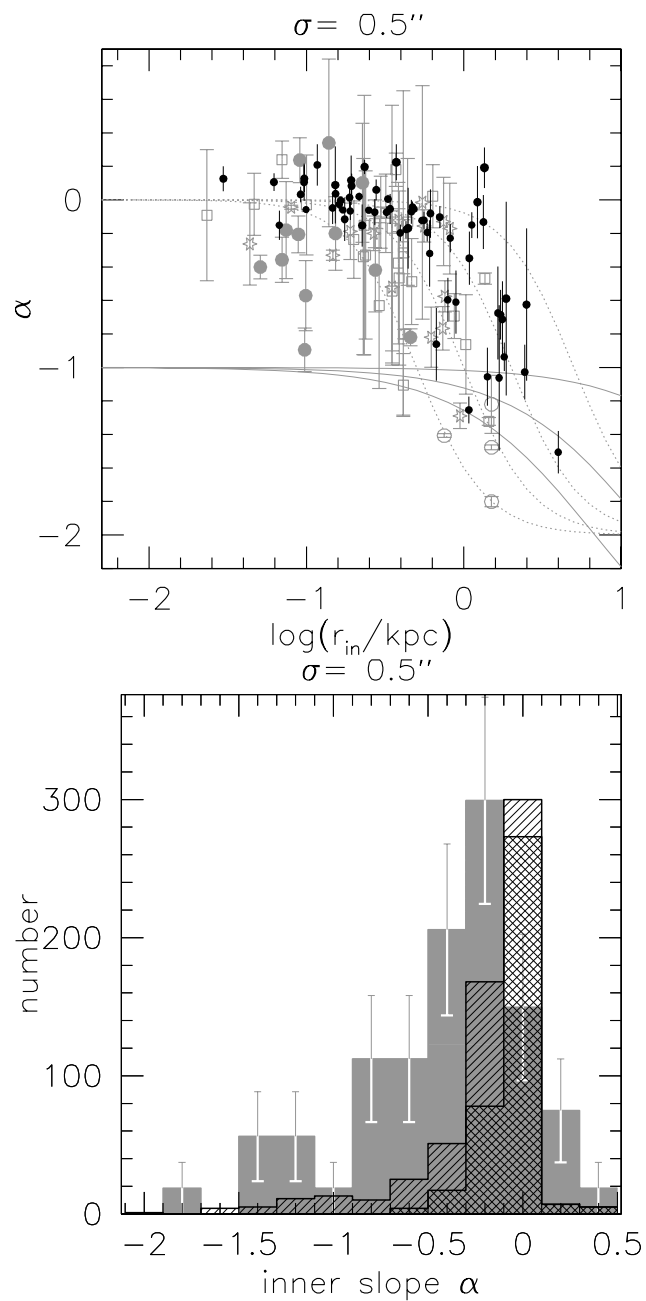


Figure 19. As Figs. 13 and 14, but now showing the results for Burkert halos. The bin at $\alpha = 0.5$ also contains galaxies with $\alpha > 0.5$.

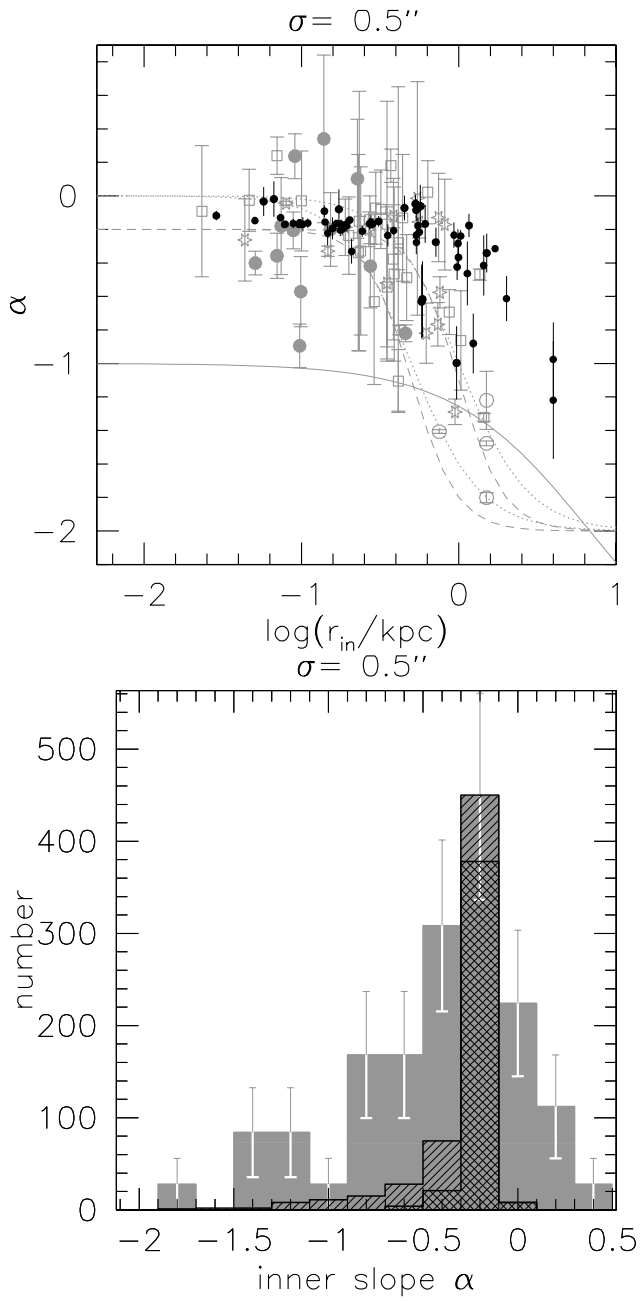


Figure 20. As Figs. 13 and 14, but now showing the results for Kravtsov halos. The bin at $\alpha = 0.5$ also contains galaxies with $\alpha > 0.5$.

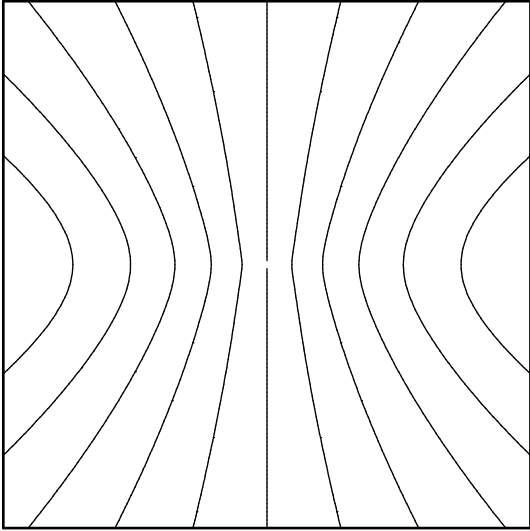


Figure 21. Velocity fields of the inner parts of massless disks embedded in a Kravtsov halo. The velocity field is seen under an inclination angle of 60° , and a position angle of 90° . The boxes measure 5×5 kpc. The vertical minor axis contour is 0 km s^{-1} , increasing in steps of 10 km s^{-1} outwards. The halo parameters are $r_0 = 3.64 \text{ kpc}$ and $V_{\text{max}} = 138 \text{ km s}^{-1}$.

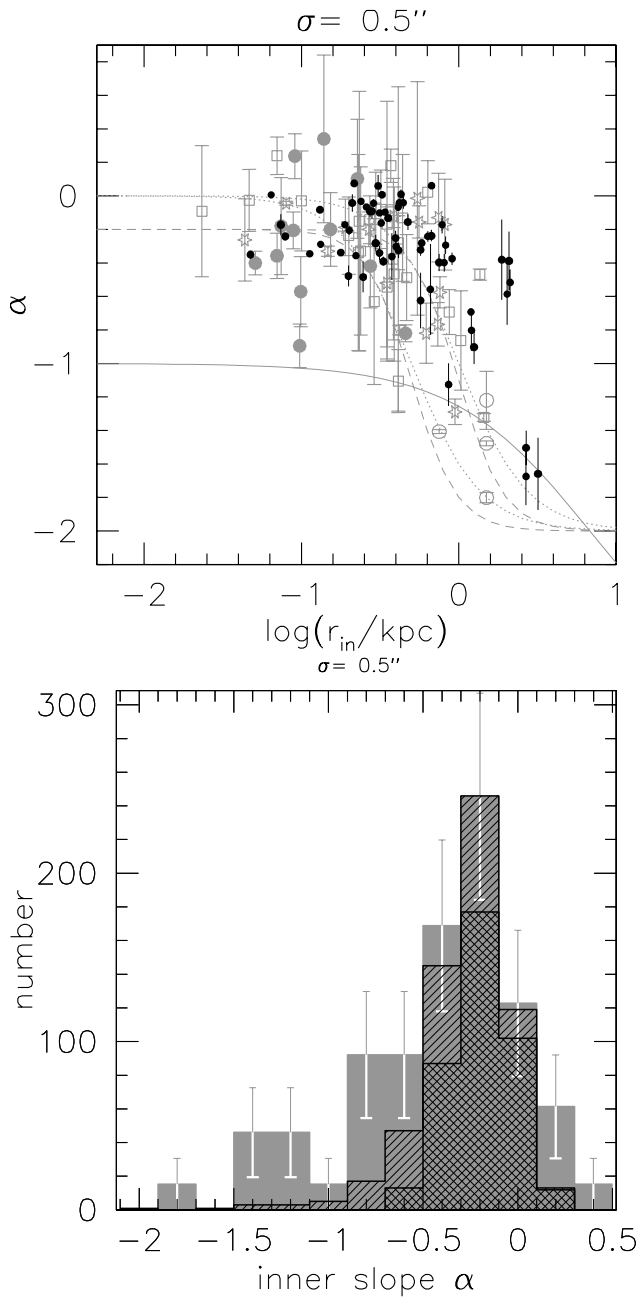


Figure 22. As Figs. 13 and 14, but now showing the results for Kravtsov halos with a $\sigma_\alpha = 0.2$ Gaussian scatter added to the value for the inner slope. The bin at $\alpha = 0.5$ also contains galaxies with $\alpha > 0.5$.

Table 1. Restricted sample

Name	Class.	Name	Class.
F583-1	U	UGC 11648	U
F583-4	U	UGC 11748	U
ESO-LV 1200211	U	DDO 64	U
ESO-LV 2060140	U	DDO 185	B
ESO-LV 3020120	B	DDO 189	U
ESO-LV 4880490	B	NGC 1560	U
UGC 731	B	NGC 4395	U
UGC 3371	U	NGC 4455	B
UGC 4325	U	UGC 11583	U
UGC 11557	D		

'B' denotes barred; 'U' unbarred; 'D' dubious